Goldstein D. B., Hedman M., Manga M., Perry M., Spitale J., and Teolis B. (2018) Enceladus plume dynamics. In *Enceladus and the Icy Moons of Saturn* (P. M. Schenk et al., eds.), pp. 175–194. Univ. of Arizona, Tucson, DOI: 10.2458/azu_uapress_9780816537075-ch005.

Enceladus Plume Dynamics: From Surface to Space

David B. Goldstein
The University of Texas at Austin

Matthew Hedman
University of Idaho

Michael Manga
University of California Berkeley

Mark Perry
Johns Hopkins University Applied Physics Laboratory

Joseph Spitale
Planetary Sciences Institute

Benjamin Teolis
Southwest Research Institute

The vapor and particulate plume rising out of Enceladus' south polar region discovered by Cassini is a dramatic and active geologic feature. This plume not only feeds the E ring but also carries information about the satellite's interior. The plume contains both jets and more distributed emissions that emerge from various fractures in the icy crust. The particle flux is tidally modulated over the course of each Enceladus day, but also appears to vary on longer and perhaps shorter timescales. Dynamically, the plume provides a thus-far-unique example of a cool multi-phase (particulates and vapor) flow into a weak gravity, vacuum environment. In this chapter we describe the plume dynamics from the continuum flow in the near-vent region, through the gas dynamic expansion process, out to the far field where vapor and particulate motions uncouple, where intermolecular collisions cease, and where the Cassini observations were made. It is ultimately those Cassini observations, interpreted through dynamical models, that will enable us to understand the source conditions for the plume.

1. INTRODUCTION

The geysers comprised of largely water vapor and icy particles feeding the broader plume over the south pole of Enceladus constitute a unique opportunity. That flow of material, moderated by several thermal and physical processes along its passage from a presumed liquid source all the way out to Cassini's orbit and beyond, provides unique access to conditions deep within the satellite. Multiple Cassini instruments [Ion and Neutral Mass Spectrometer (INMS), Cosmic Dust Analyzer (CDA), Cassini Plasma Spectrometer (CAPS), Magnetometer (MAG), Ultraviolet Imaging Spectrograph (UVIS), Visible and Infrared Imaging Spectrometer (VIMS), Imaging Science Subsystem (ISS), and Composite Infrared Spectrometer (CIRS)] characterized the gas-particle plume over and near the warm tiger stripe region. Numerous observations also exist of the near-vent regions in the visible and the IR. As described in the chapter in this volume by Spencer et al., the most likely source for these extensive eruptions is a subsurface liquid reservoir of saline water and other volatiles boiling and then escaping through crevasse-like conduits into the vacuum of space. Realistic analysis of the observations of Enceladus' plume phenomena is especially critical for making successful inferences of subsurface conditions (Spencer et al., this volume), notably concerning habitability (McKay et al. and Lunine et al., this volume). Moreover, beyond Enceladus itself, the plume injects gas and particles into Saturn's E ring and the Saturn system as a whole, influences Saturn's magnetosphere, and coats the surfaces of Enceladus and other satellites with "snow."

Both ISS and VIMS images observed Enceladus' plume via sunlight scattered by particles that are either entrained in the vapor or moving ballistically on their own (Fig. 1). The plume, as traced by the particles, clearly emanates from the tiger stripes and has both a diffuse component and many dense, narrow components, labeled "jets" or "geysers." The

scattered light intensity is greatest near Enceladus' surface and decreases with altitude over distances of hundreds of kilometers (*Hedman et al.,* 2013; *Nimmo et al.,* 2014; *Ingersoll and Ewald,* 2017). Four stellar/solar occultations observed by UVIS remotely measured the vapor, finding that the jets are of high Mach number, and can be four times denser than the diffuse components, which extend laterally only slightly beyond the region of the tiger stripes. *In situ* measurements of the gas molecules by INMS (Appendix Table A1) show densities and spatial variations consistent with UVIS. Vapor densities over the south-polar region peaked at a few times 10^8 molecules cm^{-3} at 100 km altitude and depend approximately on the altitude squared. The gas is predominately water vapor, with 1–4% other volatiles (*Waite et al.,* 2017; Postberg et al., this volume). CAPS and INMS measured ions in the plume, but, at less than 100 ions cm^{-3}, the ion density is too low to affect plume dynamics.

Individual jets and the plume as a whole show temporal variability on decadal, diurnal, and shorter timescales, presumably reflecting variations in the mass flux out of the satellite. Analyses of UVIS, INMS, and MAG data produce estimates of 100 to more than 1500 kg s^{-1} for the mass flux in vapor (although this high value is perhaps an outlier event). There is some indication in UVIS and INMS data that much of the variability occurs in the jets, with less variation in the diffuse components.

The narrowness of the vapor jets (which implies highly supersonic vapor flow) indicates that at least some of the surface vents act as converging-diverging nozzles, with vapor passing through a constriction and then rapidly expanding. Near the surface vents, the two-component flow of vapor and particles is well represented as a continuum and has well-defined pressures, densities, and species mass fractions. Within tens of meters (*Yeoh et al.,* 2015), as the plume expands to low densities and temperatures, the particles and gas no longer influence each other. At still greater distances, as the expansion continues, the gas flow transitions to the free-molecular regime, where intermolecular collisions become uncommon and both molecules and the remaining particles move ballistically, influenced predominantly by the gravity fields of Enceladus and then Saturn. Finally, at distances greater than a few hundred kilometers from Enceladus, electromagnetic effects become important; these are described in the chapter by Kempf et al. in this volume.

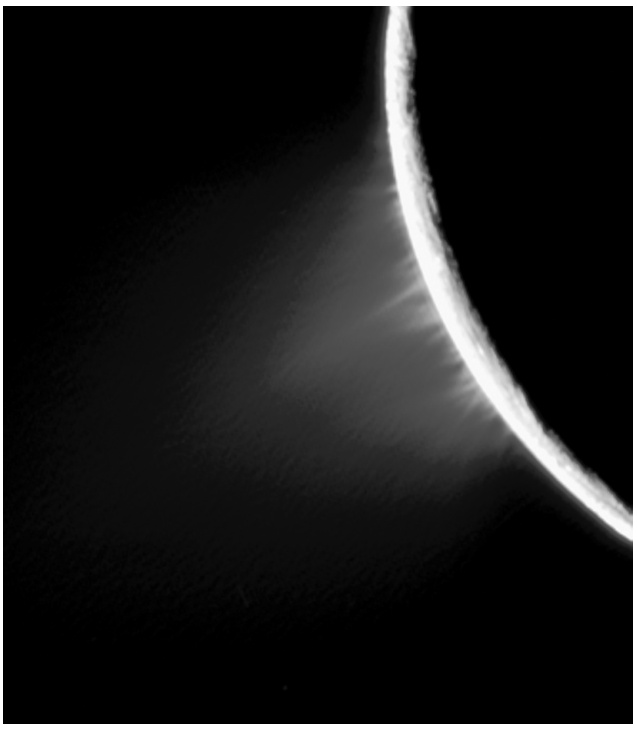

Fig. 1. See Plate 21 for color version. An ISS color-stretched image acquired on November 27, 2005, illustrating overall plume morphology threaded by many finely resolved jets or geysers.

The particulates are primarily ice grains, and vary in size, composition, and formation process. The ice grains that are seen by VIMS, ISS and CDA are on the order of 1 μm in radius and probably originate either from salty-ocean spray or from vapor condensation within the subsurface fissures (see the chapter in this volume by Postberg et al.). The CAPS instrument has measured much smaller nanometer-sized grains that presumably condense from the vapor during expansion and cooling processes. CIRS finds that the surface temperatures increase with proximity to the tiger stripes and reach 170 K at the hottest regions, but the expansion cools the plume vapor to less than 30 K above the surface (*Yeoh et al.,* 2015).

The suggested Europa south polar plume (*Roth et al.,* 2013; *Sparks et al.,* 2016) may be similar to Enceladus in all but the gravity field and net mass flow. At the other end of the spectrum, cometary plumes are similar to the Enceladus plume in terms of their gas/particulate dynamics, constituents, mass flow, velocities, and exhaust into vacuum, but differ in their driving source mechanisms.

One of the most intriguing aspects of the Enceladus plume is its potential link to extraterrestrial habitability and the search for life elsewhere in the solar system. If the plume constituents ultimately arise from a liquid water source, the plume may present an exceptional and unique opportunity to examine and sample liquid water constituents from deep within a surface-frozen ocean world. Important questions then relate to how those constituents, whether molecular indicators or even possibly entire organisms, were processed below the surface and within the plume on the way to their examination (see the chapters in this volume by McKay et al. and Lunine et al.).

Below, we first describe the visible and measurable aspect of the plumes and their source — the tiger stripes — in section 2. Section 3 describes the observed temporal variability and some of the possible controlling mechanisms. Section 4 discusses the processes encountered as the subsurface water becomes the vapor and the ice grains that escape from the surface vents. Once we have begun to detail the physics of the Enceladus plume, we take a brief diversion in section 5 to set this plume into the context of other observed related

plumes in the solar system. Sections 6 and 7 examine the physical properties of the emitted particles and vapor from the surface to hundreds of kilometers, where they transition to the environment external to Enceladus.

2. VENT LOCATIONS: TIGER STRIPES, STRONG JETS, DISTRIBUTED SOURCES, JET RELATIONSHIPS TO THERMAL OUTPUT

2.1. Analysis of Initial Observations

While the material emerging from the south pole has been observed with multiple instruments, the most detailed information about the source locations comes from the ISS observations, which include highly resolved observations of the particle-rich jets from the tiger stripe fissures. In 2005, ISS observations revealed large rifts in the crust, informally called "tiger stripes" (*Porco et al.,* 2006). These fractures (each of which comprises numerous branches) are named Alexandria, Cairo, Baghdad, and Damascus (Fig. 2), and were hypothesized to be the sources of the observed jets. That hypothesis was supported by Cassini CIRS observations (*Spencer et al.,* 2006), which detected anomalously high temperatures (~85 K) south of 65°S latitude, and identified several localized regions (labeled A–F in Fig. 2) of particularly high temperatures (~145 K) along the tiger stripe fractures.

Triangulating ISS observations of jets taken between 2005 and 2007, *Spitale and Porco* (2007) inferred the positions of eight major jet sources. Those triangulations were performed by representing jets in images as line segments and identifying clusters of intersections that simultaneously yielded common geographic source locations and direction vectors. Many of the resulting source locations, labeled I through VIII (Fig. 2), coincided with the *Spencer et al.* (2006) CIRS hot spots, and all of them were consistent with emission from the tiger stripe fractures.

In *Spitale and Porco* (2007), the observations that contributed to each solution were mostly taken from large distances, and occurred over multiple Cassini orbits. As a result, that approach characterized the prominent collimated jets (or concentrations of unresolved fine jets) that could be seen from large distances, and which remained reasonably static during the intervals between those observations, which were typically months or more. Because of the large distances, the precision of the inferred source locations was typically no better than 10 to 20 km, sufficient to distinguish which tiger stripe was involved, but not necessarily which branch.

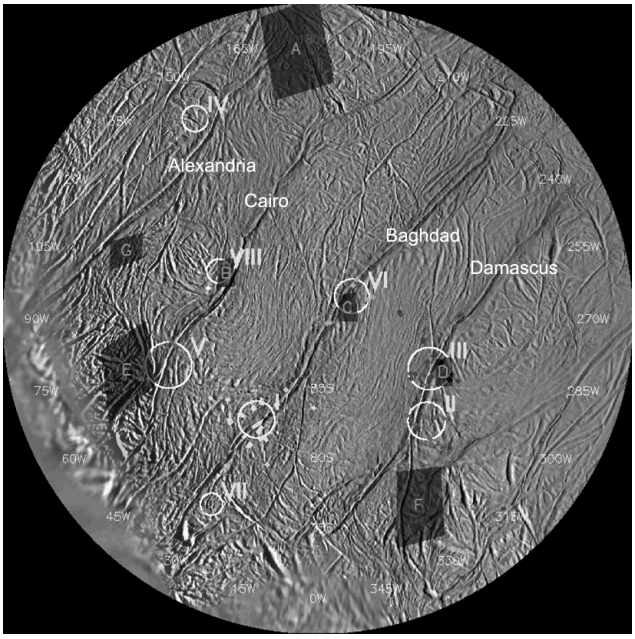

Fig. 2. See Plate 22 for color version. Polar stereographic projection of Enceladus' south polar region showing the eight source locations inferred by *Spitale and Porco* (2007) using triangulation. Locations of CIRS hot spots from *Spencer et al.* (2006) are shown as red quadrilaterals.

2.2. Analysis of High-Resolution Observations

Understanding the time variability of the jetting activity over the south polar terrain (important in determining the connection with tides; see section 3 below) required significantly better spatial and temporal resolution than provided by the 2004–2006 images used in *Spitale and Porco* (2007). To that end, a new series of observations was conducted at distances that enabled resolution of the fine structure of the jets and provided sufficient parallax to perform triangulation during a single encounter.

Porco et al. (2014) analyzed those new observations (Fig. 3 is an example) using an updated triangulation approach. Approximately 100 sources were inferred, and maps of jetting activity at various times were produced (Fig. 4). The geographical distribution of the inferred jetting activity was shown to be consistent with CIRS temperatures (*Howett et al.,* 2011) and with localized hot spots seen in high-resolution Cassini VIMS observations (*Goguen et al.,* 2013). The possibility of lower-speed eruptions forming sheets of material was left as an open question by *Porco et al.* (2014). Many of the inferred jets were observed be in various states of activity in different observations, although a tidally controlled relationship (*Hurford et al.,* 2007) was not apparent.

Spitale et al. (2015) analyzed several of those same datasets using a different approach. The motivation for developing a different approach was that much of the activity (per unit length of tiger stripe fracture) appears as a continuous glow rather than as discrete jets that can be represented as simple lines in an image. Moreover, much of the fine discrete structure that does appear is difficult to reliably identify among successive images. In this approach, active regions were located by comparing a *simulated curtain* of material with the emission seen in an image. The simulated curtain could emerge at any zenith angle, and linear spreading with altitude could also be included. Because those observations were obtained during the onset of southern winter, most of the source locations were in shadow, and the shadow of

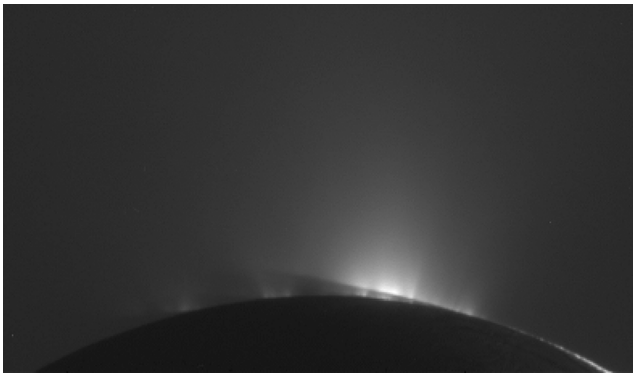

Fig. 3. Cassini ISS image showing Enceladus' shadow cast on the planes of material associated with each tiger stripe.

Enceladus was cast across the emerging jets (Fig. 3). In many cases, those shadows allowed for the unique identification of the active fracture associated with a given curtain of observed material.

Spitale et al. (2015) produced two notable results: (1) Maps of activity at five different times (Fig. 5) spanning about a year showed that most of the fracture system is active at all times. (2) It was noted that jet-like artifacts (referred to as phantom jets) may appear in a simulated image due to a fortuitous combination of the viewing angle relative to the fracture geometry (Fig. 6).

Results corroborate the geographic link between eruptive activity and elevated CIRS temperatures that was first established by *Spitale and Porco* (2007) and expanded by *Porco et al.* (2014). Moreover, activity was detected on fractures for which CIRS has not shown elevated temperatures; in particular, the fracture system branching from Baghdad Sulcus at Source VI was seen to be active on day 2010-225.

The *Spitale et al.* (2015) result (point 2 above) may explain why many fine features are difficult to reliably identify throughout an imaging sequence as the geometry varies. *Spitale et al.* (2015) also suggested that some of the *Porco et al.* (2014) jets may not be real jets but instead ripples in a curtain of emission. On the other hand, *Porco et al.* (2015) have pointed out that 90 to 95 of the 98 jets were triangulated on the basis of images from a wide range of viewing angles at >45° (*Porco et al.,* 2014) to the tiger stripes, lending confidence to their identification as real jets. Indeed, *Helfenstein and Porco* (2015) have identified a number of surface features corresponding to *Porco et al.* (2014) solutions that support the eruption of discrete jets at those locations (see below). Moreover, some discrete jets may have been missed because they spread out and blend with their neighbors before emerging into the sunlight, appearing as continuous curtains.

2.3. Jets and Curtains

It is likely that both jet and curtain eruptive styles coexist, may be end members of the same phenomenon, and reflect different effects of the geology and the dynamics of the Enceladus system. Presumably, there exists a distribution of vent aspect ratios (length:width) with round holes having a value of 1.0 and long slots having a value approaching infinity. Due to their great heights, the features measured by *Spitale and Porco* (2007) are almost certainly supersonic jets with embedded particles that feed the E ring and do not fall out directly onto the surface of Enceladus. Many of the most convincing *Porco et al.* (2014) jets are bright to high altitudes and also likely fall into this category. Indeed, *Mitchell et al.* (2015) were able to reproduce the "tendril" structures in Enceladus' E ring using the fastest particles launched from the most active *Porco et al.* (2014) jets. The

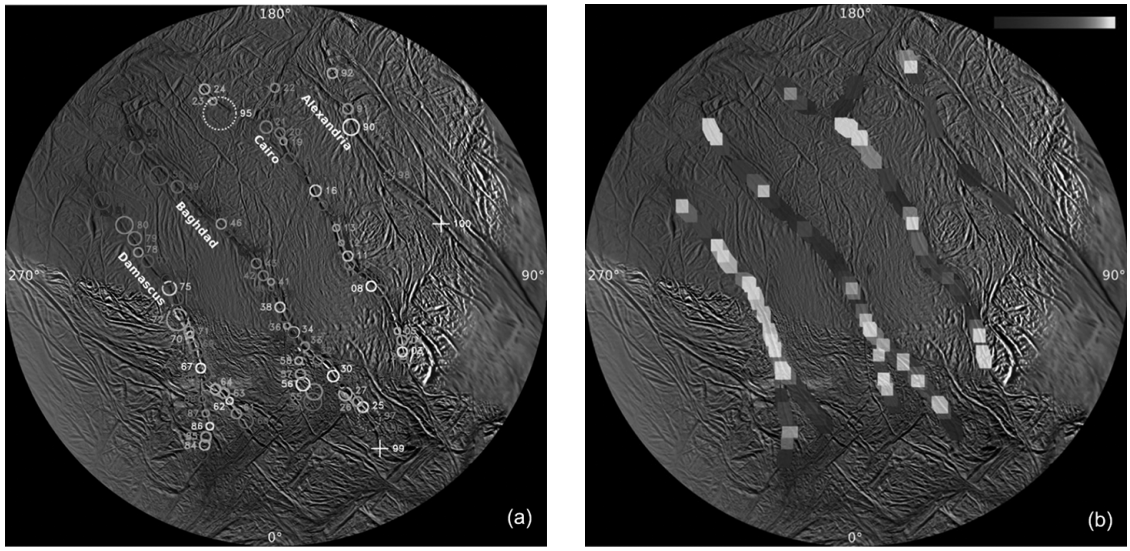

Fig. 4. See Plate 23 for color version. **(a)** Locations of the jets. **(b)** Jet activity derived from ISS observations. There is strong correlation with the jet activity and the tiger-stripe temperatures measured by CIRS and VIMS. From *Porco et al.* (2014).

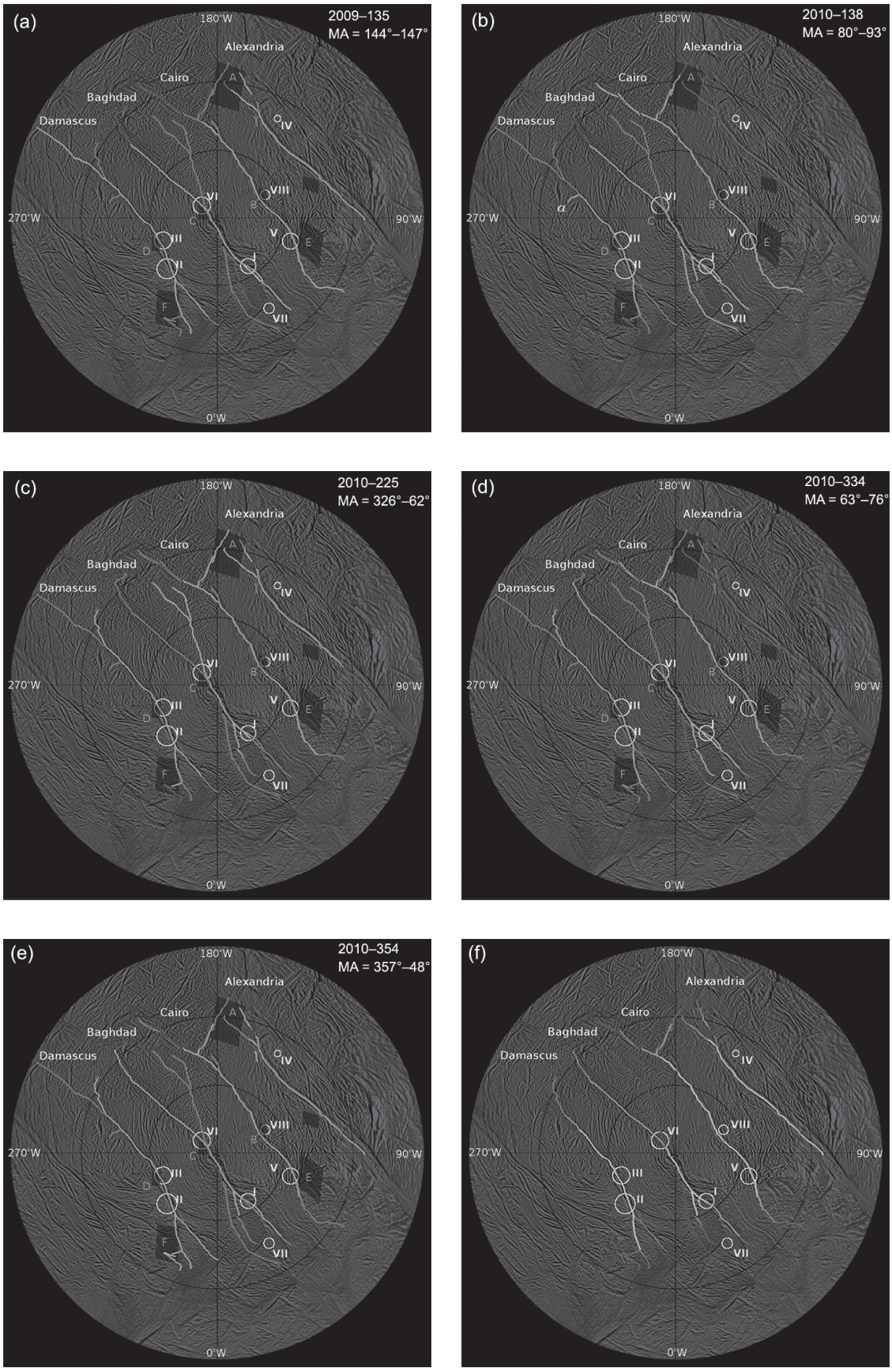

Fig. 5. See Plate 24 for color version. Curtain activity at five different mean anomalies (MA), and the average (f). Green areas are active, red areas are inactive, and blue areas are undetermined.

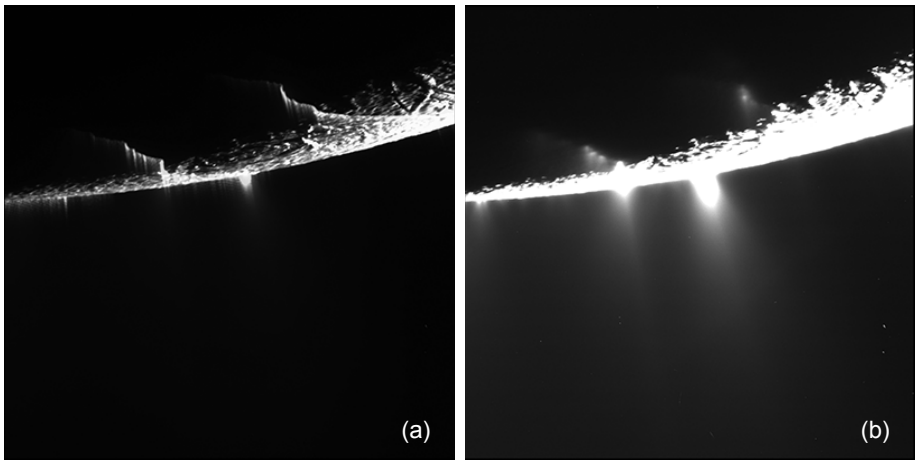

Fig. 6. Curtain simulation overlain on image N1637461416. **(a)** Image is displayed with no overlay, and stretched to make the erupted material visible. **(b)** Image is displayed with no stretch, with simulated curtains overlain. The simulated curtains are sampled *uniformly* at 250-m intervals along each fracture, and the ground-level intensities are also uniform. "Phantom" jets appear at locations where the line of sight intersects the curtain at a shallower angle than in the immediate surroundings. Every relatively bright feature in the simulated curtain is a phantom; note the correspondence with apparent "jets" in the Cassini image. Nightward of the terminator, the bottom edge of the curtains are defined by the shadow of Enceladus, allowing the unique determination of the source fractures.

curtain-like sprays, on the other hand, tend to have heights closer to 10 km and likely consist of material launched at lower velocities. That hypothesis is supported by simulations (*Kempf et al.,* 2010) comparing the fallout patterns for initial conditions corresponding to *Porco et al.* (2014) jets and those for *Spitale et al.* (2015) curtains to the observed albedo pattern on Enceladus' surface.

In addition to feeding the E ring, the supersonic jets identified in *Spitale and Porco* (2007) and *Porco et al.* (2014) likely account for most of the tidally-modulated emission noted by *Hedman et al.* (2013) (section 3 below), as those observations covered altitudes from 50 to 450 km. At lower altitudes, where the curtains may dominate, a tidal signature has yet to be discovered in the ISS data.

2.4. Correlation with Geology and Morphology

The broad correlation between jetting activity and prominent fractures in the south polar terrain has been thoroughly established based on imaging of the region at moderate resolutions (*Porco et al.,* 2015). Coverage of the region at the very high resolutions needed to associate jetting activity with local morphological features is incomplete, although some intriguing associations have emerged. *Helfenstein and Porco* (2015) examined the very-high-resolution Cassini images and found that (1) azimuths of the jets align preferentially with the main fractures, local cross-cutting fractures, or a local tectonic fabric; and (2) some *Porco et al.* (2014) source locations correspond to local features suggestive of ballistic fallout, scouring, or other processes that create radial striations and/or buildups centered at locations on the primary fractures [see Fig. 7, as well as Fig. 16c of *Helfenstein and Porco* (2015)].

One difficulty with result 1 above is that multiple directions of cross-cutting are apparent in some surface images, and other fractures may exist that would only be discerned at higher resolutions than those available, reducing the statistical significance of any directional correlation. However, if a variety of orientations are available to respond to the rotating stress field at a particular locale, vapor may be emitted with different orientations at different times, and it might explain why low-altitude activity is seen at some level throughout the tidal cycle.

Approximately 20% of the jets that do not appear to align preferentially with fractures or tectonic fabric may align with unresolved fractures, or their existence may argue against the proposed correlation. They also may be evidence for phantoms in the *Porco et al.* (2014) solutions, although the 57 jets examined in the *Helfenstein and Porco* (2015) study were selected for their prominence and consistent non-zero zenith angles, conditions that appear to favor real discrete jets. Those conditions also favor the supersonic jets that likely contribute to the high-altitude plume, which is tidally modulated. The strong correlation of the density of the high-altitude plume with mean anomaly implies a response to a consistent fracture orientation, potentially in conflict with the idea of a significant contribution from fractures not aligned with primary fracture system.

The association of morphologic features with *Porco et al.* (2014) jet solutions in result 2 above (Fig. 7) provides strong confirmation for those features being physical jets, and provides a window into the jetting mechanism at the surface. The appearance of these features, particularly the radial striations, does not lend itself to other obvious explanations, but a systematic analysis of the correlation between jet solutions and morphologic features has yet to be performed.

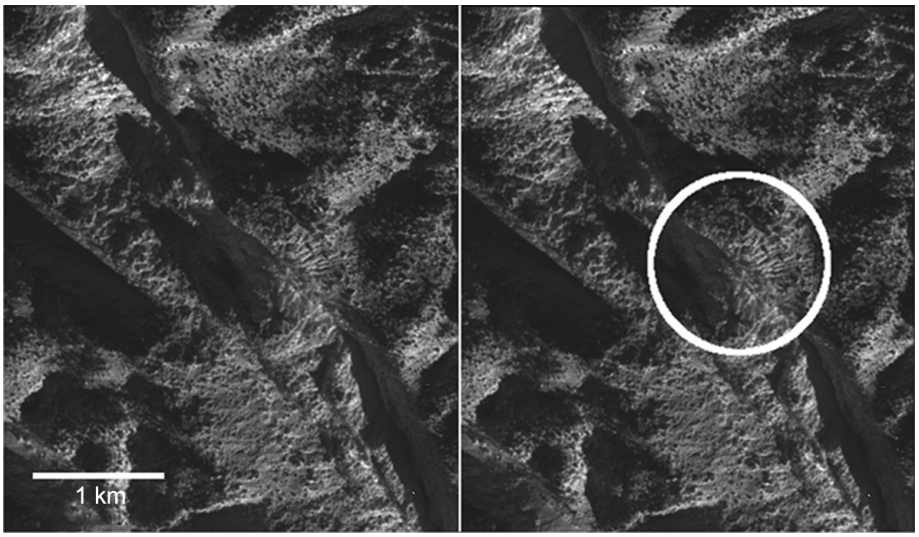

Fig. 7. Radial striations emanating from Baghdad Sulcus suggesting localized emission. From *Helfenstein and Porco* (2015).

3. TIME VARIABILITY OF JETS AND THE PLUME: PRESUMED PROCESSES AND THEIR RELATION TO THE ORBITAL DYNAMICS OF ENCELADUS

The sources of Enceladus' plume material not only have a complex distribution in space, they also vary significantly with time over periods ranging from days to years. Thus far, the best-documented temporal variations are periodic changes in the plume's total particle output that are correlated with the satellite's location on its orbit around Saturn. Enceladus' orbit is not a perfect circle, so both the distance between Enceladus and Saturn and Enceladus' orbital velocity oscillate back and forth slightly during the satellite's 33-hour orbit. As discussed in the chapters in Part 1 of this volume, these small oscillations change the tidal stresses across the south polar terrain, altering the connections between the plume vents and the subsurface and thus influencing the satellite's plume activity.

Two instruments onboard the Cassini spacecraft have detected particle-output variations that are clearly correlated with Enceladus' location along its eccentric orbit: the cameras of ISS (*Nimmo et al.,* 2014; *Porco et al.,* 2014; *Ingersoll and Ewald,* 2017) and VIMS (*Hedman et al.,* 2013). Both instruments obtained images of the micrometer-sized particles erupting from the satellite over a wide range of times and observing conditions. The apparent brightness of the plume in these datasets depends upon both the number density of plume particles and the viewing geometry, particularly the phase angle (i.e., the Sun-plume-camera angle). This angle is important because the particles in the plume scatter light more efficiently at higher phase angles, and so the same material appears brighter when the phase angle is larger. Fortunately, these viewing-geometry-dependent variations can be determined by comparing observations at the same phase angle and/or by applying appropriate corrections based on light-scattering models.

In practice, different authors have used different methods of estimating the dependence of the plume's brightness on phase angle. *Hedman et al.* (2013) used a simple correction where the plume's brightness was a power-law function of the scattering angle, which was based on the observed variations in the plume's brightness at different orbital phases. *Nimmo et al.* (2014) used a more complex phase function that was computed using Mie theory and the particle-size distributions of the plume particles derived from VIMS spectra (*Hedman et al.,* 2009). Finally, *Ingersoll and Ewald* (2017) used several different phase functions derived by *Gao et al.* (2016) that were extrapolated from an earlier study of extremely high-phase plume observations (*Ingersoll and Ewald,* 2011). The *Hedman et al.* (2013) approach has the advantage of being simple, but since the assumed phase function was derived from the VIMS data by assuming that the plume always had the same brightness at a given orbital phase, and since different phase angles were observed at different times, there is a chance that this method would suppress long-term trends in VIMS measurements of the plume's brightness. By contrast, the other methods assume that measurements of the plume's spectra and/or phase function measured at one time can be extrapolated and applied to all the other observations. A potential problem with the latter approach is that it assumes that the physics of the flow/particles remains unchanged — it is just that the mass flow changes between observations. While all these methods do yield similar results, i.e., the relative variation with mean anomaly is well established, there are differences in the detailed trends that will probably require more indepth investigations of the plume's photometry before they can be resolved.

Figure 8 shows the ISS and VIMS estimates of the plume's ice-grain output — corrected for viewing geometry — as functions of the satellite's position along its orbit. Both sets of data clearly show that the plume's ice-particle output is roughly four times higher when the satellite is furthest from Saturn than it is at other points in its orbit. This trend is repeatable among different subsets of the data and is not linked to other phenomena such as shadowing by Saturn, and therefore appears to be a persistent feature of Enceladus' geological activity for the duration of the Cassini mission.

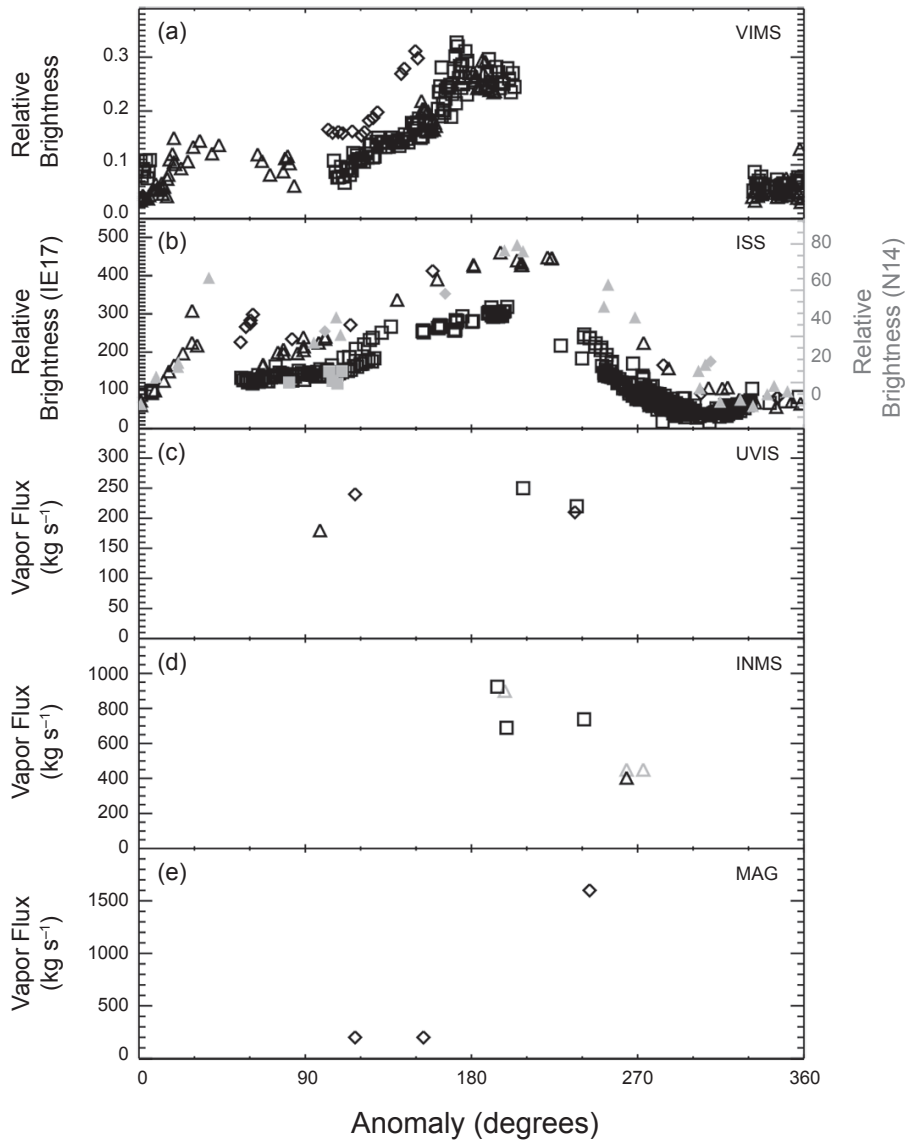

Fig. 8. Temporal variations in Enceladus' plume activity as observed by various Cassini instruments. All panels show a measure of plume activity as a function of the satellite's orbital anomaly (an anomaly of 0° corresponds to when the satellite is closest to Saturn, and 180° is when the satellite is farthest from the planet). **(a)** VIMS estimates of the plume's brightness at 85 km altitude and 1.2 μm, corrected for phase angle (*Hedman et al.,* 2013). **(b)** Estimates of the plumes' brightness derived from ISS images by *Nimmo et al.* (2014) (gray) and *Ingersoll and Ewald* (2017) (black). **(c)** Estimates of the gas flux derived from UVIS occultations using the UVIS-derived Mach number for vapor spreading with a temperature of 170 K (*Hansen et al.,* 2017). **(d)** Gas fluxes derived from INMS data obtained during several flybys by *Yeoh et al.* (2017) (E3, E5, and E7 flybys in gray) and *Teolis et al.* (2017) (E7, E14, E17, and E18 "adiabatic" estimates in black). **(e)** Estimates of the gas flux derived from MAG data from the E0, E1, and E2 flybys by *Saur et al.* (2008). In all five panels, different symbols correspond to different observation times: Measurements marked with diamonds were obtained before 2008, those marked with triangles were obtained in 2008 through 2010, and those marked with squares were obtained in 2011 through 2016. The VIMS measurements and the two ISS analyses show clear increases in the plume's brightness as the satellite moves through anomalies of 180°. There is also evidence that the plume's overall activity level has decreased over time. Differences in the shapes and magnitudes of these trends may in part reflect differences in how the VIMS and ISS groups corrected for variations in the observed phase angle. While the UVIS data show comparatively little variation in the gas flux, the MAG and INMS analyses could indicate higher gas fluxes when the satellite is near apoapsis.

This implies that changing tidal stresses are producing repeatable physical changes below the surface of Enceladus.

Interestingly, while the total flux of particles from Enceladus changes dramatically as the satellite moves around Saturn, the vertical structure of the plume does not change nearly as much. Again, direct comparisons of the published analyses are challenging because different authors used different models for the plume's vertical structure. For example, *Nimmo et al.* (2014) fit an exponential vertical profile to integrated brightness observations and reported a nearly constant scale

height parameter. *Hedman et al.* (2013), by contrast, found a linear trend better described the particle velocity distribution and found the effective maximum velocity is 10% smaller when the satellite is near its orbital apoapsis and the particle flux is highest. Finally, *Ingersoll and Ewald* (2017) argued that the plume's brightness decayed with altitude like a power law, and that the power-law index was larger (~–0.4) when Enceladus was near its orbital apoapsis and smaller (~–0.2) at other orbital phases. Note that despite their different ways of parameterizing the trends, both the *Hedman et al.* (2013) and *Ingersoll and Ewald* (2017) analyses suggest that the plume's brightness variation with altitude, as derived from ISS data, declines more quickly when Enceladus' activity level is high. Since the visible plume particles follow nearly ballistic trajectories (see below), this implies that the launch velocity distribution of the plume particles is steeper when Enceladus is near its orbital apoapsis. However, the velocity distribution of the particles does not change as dramatically as the particle output. These trends probably reflect changes in the fissures driven by the changing tidal forces (see the chapters in Part 1 of this volume), but the subtlety of the velocity distribution changes also places stringent limits on the degree to which tidal forces can change the geometry of source vents (see section 6).

The gas flux also varies, but its behavior is less well characterized than that of the particles. The first and largest variations in gas flux were described by *Saur et al.* (2008), who attributed variations in the magnetometer data from the first three Enceladus encounters to flux decrease from 1600 kg s^{-1} for E0 (orbit phase of 230°) to 200 kg s^{-1} for E1 (orbit phase of 160°) and E2 (orbit phase of 110°). This early analysis did not incorporate some of the later knowledge of the plume, including the large component of charged dust, and that may explain the E0 flux, which is larger than other measurements. The first INMS data that were sufficient for mass-flow analyses were E3 (270°) and E5 (200°), which showed more-modest variations in vapor flow [*Smith et al.* (2010) found a factor of 4 difference between E3 and E5; *Dong et al.* (2011) and *Yeoh et al.* (2017) found a factor of 2] that were consistent with the particle-flux orbit-dependent variations. [Analyses of later INMS data, particularly E14, E17, and E18, which had parallel trajectories, also showed variations that correlated to orbit phase (*Perry et al.,* 2015).] These INMS total-inferred flow rates depend heavily on modeling, as INMS only measures gas density along a single instantaneous line through the plume. In contrast, the UV occultations provide an integrated sampling across nearly the entire plume, providing column density, but assume a gas velocity to obtain a gas mass flux. The first three UV occultations, which all occurred during the low-grain-output phase of Enceladus' orbit, showed little variation in the plume gas flux output (*Hansen et al.,* 2011). The fourth and last occultation (*Hansen et al.,* 2017) occurred closer to Enceladus' apoapsis. Although the total column density was similar to previous UVIS measurements, there is indication that the stronger, narrow jets were denser than during previous measurements (*Hansen et al.,* 2017). A tentative explanation is that the diurnal variations of the prominent jets are greater than those of the broader plume. Since vapor velocity was not measured directly in these analyses, most of them [*Saur et al.* (2008) is an exception] required an assumed temperature to convert the derived Mach number to total flux. As discussed in the chapter by Smith et al. in this volume, the total mass of the E-ring neutral torus provides an additional constraint on the time-averaged vapor flux from Enceladus.

The changes in the plume's overall particle output on orbital timescales may be the best-understood variations in Enceladus' geological activity. Furthermore, the observed activities of particular sources do not show any apparent correlation to orbital phase or tidal stress state (*Hurford et al.,* 2012). This suggests that while the overall particle flux from the plume can exhibit very regular behavior associated with orbital position over several years, individual sources and vents can turn on and off in a much more stochastic manner. In this context, it is worth noting that *Roddier et al.* (1998) described a bright streak in the E ring in 1995 telescopic observations that could potentially represent a major outburst of material from Enceladus, the likes of which has never been observed by Cassini.

On longer timescales, it appears that the plume's activity level, as measured by the particle flux, has decreased over the course of the Cassini mission, being between 50% and 100% higher prior to 2008 than it has been since that time (*Hedman et al.,* 2013; *Ingersoll and Ewald,* 2017). This could represent a slow decrease in Enceladus' activity driven by the progressive choking off of various vents, but the magnitude of the decrease makes this idea problematic because it would imply that Enceladus will stop venting material entirely in a few more years, and the persistence of the E ring suggests that Enceladus' output has persisted in some form for decades. Instead, it seems more likely that the slow decrease is part of some long-term cycle in plume activity. Two mechanisms that might be involved in this are the 11-year variations in Enceladus' orbital eccentricity (which may influence tidal stresses) (*Ingersoll and Ewald,* 2017) and seasonal changes in the solar illumination at the south pole (which may affect thermal stresses in the near-surface crust). Note that the eccentricity variations are very small, and so it is unclear if they can significantly affect plume activity, and no one has yet evaluated whether solar heating can significantly affect the plume output given that the relevant thermal wave can only penetrate a few meters below the surface.

4. TRANSITION TO/FROM WATER TO VAPOR/GRAINS ABOVE THE SURFACE: NOZZLE FLOWS, PARTICLE DISTRIBUTIONS NEAR THE JETS, AND THERMODYNAMICS

We now begin a discussion of the gas- and grain-dynamics. To provide context, Fig. 9 illustrates features and dominant physics expected in different regions in the eruption. At region A, which is well below the surface, there is liquid, yielding droplets and vapor that make their way to the surface as described in the chapter by Spencer et al. in this

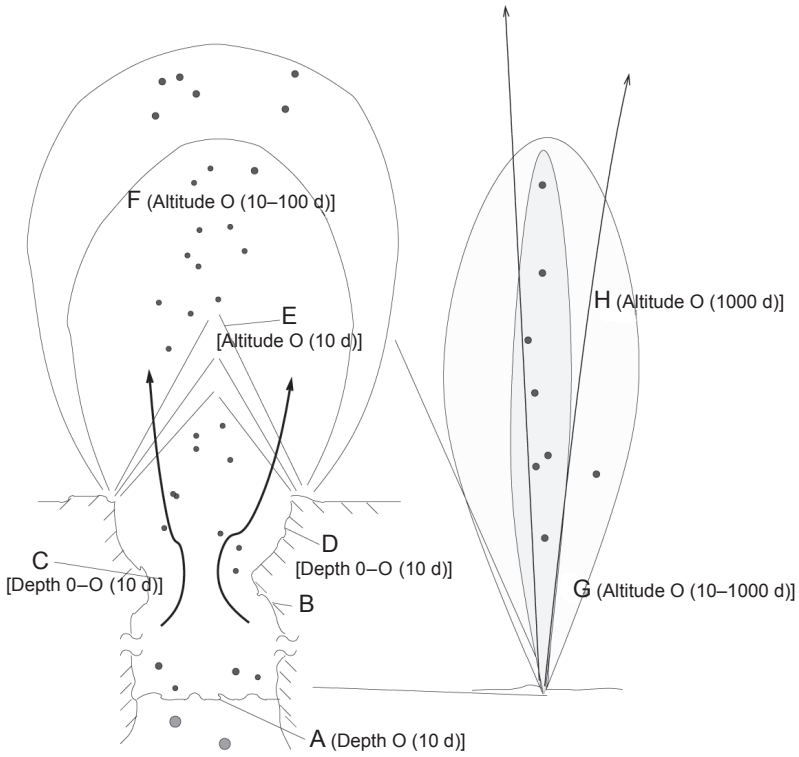

Fig. 9. Schematic drawing of the features and regions of dominant physics (A–H described in the text) of a geyser. The depth or altitude of the region is given in terms of an order of magnitude multiple of vent diameters (d).

volume. As the mixture of vapor and particles approaches the surface (region B), it has been moving slowly but can accelerate through a constriction or gas-dynamic throat and continue expanding and accelerating below the surface (region C) due to an increase in conduit cross section or perhaps due to condensation on the sidewalls. In region D (discussed in this section), the flow may still be interacting with the icy conduit via heat, mass, and momentum exchange. Once above the surface (section 6), the gas/particulate flow will pass through expansion waves (region E). There will be a continuing conversion of thermal energy to directed energy as the gas accelerates upward from the surface and cools. As the above-surface geyser continues to expand, the gas and particulate densities drop (region F). There is no background atmosphere to interfere with the plume expansion into vacuum. The particulate motion will decouple from the vapor motion in region G (*Yeoh et al.,* 2015), and some particulates can fall back to the surface. Even further above the vent (region H; see section 7), the mean free path length for intermolecular collisions increases to tens of kilometers and molecules and particles thereafter follow ballistic trajectories subject to only gravitational and, when ionized, electromagnetic forces. All Cassini actual observations of aloft gas and particles occurred near and above region G where the particles and vapor had already parted ways.

As the subsurface two-phase flow approaches and broaches the satellite's surface it will expand rapidly (Fig. 9, region D). Due to the rapidity of the final stage of the expansion, it is a good approximation that the process is adiabatic — there is no energy exchange via conduction or radiation between the flow and the surrounding conduit sidewalls. If the flow is sufficiently rapid, the time is too short for equilibration of vapor pressure with the sidewalls. It is presently unclear if the process of vapor pressure equilibration would be causing condensation or sublimation of sidewall ice right near the exit — it depends on the exact details of surface temperature, vent geometry, and gas dynamics and detailed simulations coupling all of the relevant physics have not been done (see discussions in *Ingersoll and Nakajima,* 2016; *Nakajima and Ingersoll,* 2016).

If the flow *is* adiabatic and mass exchange between the gas and the sidewalls at the exit is negligible, the vent will act as a nozzle through which the flow expands to supersonic speeds, as has been suggested by the narrowness of the jets (*Hansen et al.,* 2011). In an ideally designed rocket nozzle meant for operation with gas flows into the vacuum of space, the flow is *sonic* at the narrowest area (the throat). Sonic conditions mean the flow speed is equal to the local speed of sound, $\sqrt{\gamma RT}$ if the flow is of an ideal gas, where γ is the ratio of specific heats and R the gas constant [and perhaps less if it contains even a modest mass fraction of particles; e.g., if the particulate mass loading is 10% and the grains move with the gas in complete gas-particle equilibrium, the speed of sound is reduced by ~8% (*Kieffer,* 1982; *Kilegel,* 1966)]. Once past, the throat flow expands to high speed at the exit while moving straight out of the nozzle along its axis. In a less-than-ideal nozzle, there are viscous losses of flow momentum that may cause shock waves, flow separa-

tion from the nozzle walls, and condensation. Also, if the length of the nozzle is insufficient to accelerate the flow to near zero temperature (at which point all thermal energy in the flow has been converted into directed kinetic energy), the exit plane Mach number will be finite and the gas (but not the particles) will continue to expand laterally and axially even after it leaves the nozzle. Presumably, the actual Enceladus vents are not ideal and the finite exit Mach number flow will continue to expand above the surface. Since the processes that cause temporal variability in particle output have less than a 10% effect on particle speed (Fig. 10), those processes may occur below any gas dynamic throat because the exit-plane velocity and Mach number are determined by the throat-to-exit area ratio.

The phase diagram of water for low temperatures and entropies, Fig. 11, provides insight into some of the processes controlling the mass fractions of ice and vapor that enter the plume. If the plume is supplied by liquid water transported in near local thermodynamic equilibrium directly from an ocean at close to 273 K (red circle in Fig. 11), only a few percent of the mass of the plume would be vapor, assuming decompression following either the red or green curves in Fig. 11 ends at ~190 K due to kinetic limitations when temperature and density are low and gas velocity is high (p. 459 in *Lu and Kieffer,* 2009). But the *observed* mass fraction of vapor appears to be 90–95% (e.g., *Gao et al.,* 2016), although this value is poorly constrained and is certainly dependent on exactly where one looks within the plume. Still, one-way flow of ocean water into a thermodynamically equilibrium plume is incompatible with the observed ice/water ratio derived from Cassini measurements, and there must therefore be some process of circulation or overturning in the plumbing system to recycle liquid that then does not erupt as vapor (e.g., *Postberg et al.,* 2011; *Kite and Rubin,* 2016; *Ingersoll and Nakajima,* 2016) and/or removal combined with ballistic return of solid ice in the lower portions of the jets and plume. These general conclusions should not differ much if the water is salty because the dissolved salts do not change the thermodynamic properties of water significantly. However, the presence of salt does change the temperature-dependence of liquid density, which in turn affects convection and freezing of liquid in the vent (*Ingersoll and Nakajima,* 2016).

The height to which particles are ejected and hence how plume brightness decays with altitude, the scale height, depends on the particle-size distribution and the square root of the eruption speed of particles at the vent. If that scale height does not change over time (*Hedman et al.,* 2009; *Nimmo et al.,* 2014; *Ingersoll and Ewald,* 2016) or vary with integrated brightness for numerous different Cassini images, the implications are that there is a constant velocity distribution for visible particles and a constant particle-size distribution. This observation is consistent with the hypothesis that the flow emerging from the vents is choked to the speed of sound of the gas-and-solid mixture. One interpretation is that the integrated brightness is proportional to the cross-sectional area of the throats of the vents feeding the eruptions and the Mach number is very high: Since brightness varies by a factor of ~4 throughout the orbital cycle, the open throat area thereby also varies by a factor of ~4.

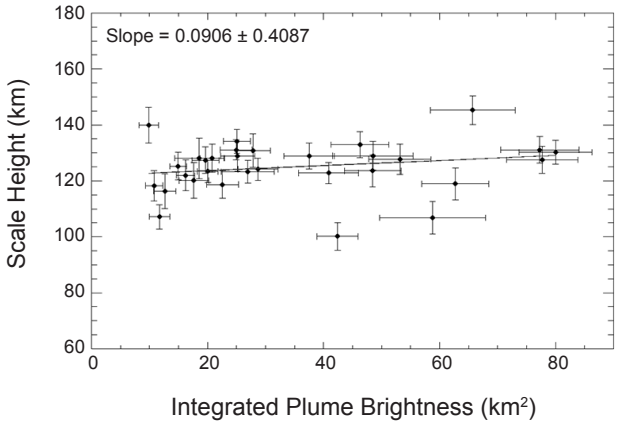

Fig. 10. Plume scale height, obtained assuming brightness decays exponentially with height, vs. integrated plume brightness from many ISS images (*Nimmo et al.,* 2014). The analysis is based on I/F measurements for altitudes from 50 km to 500 km. An early analysis (*Porco et al.,* 2006) found a scale height of 30 km when analyzing data from the surface to 50 km. This difference could be due to the larger, slower, bound particles that dominate the lower altitudes (*Postberg et al.,* 2011; *Hedman et al.,* 2009) and that brightness does not decay exponentially with height (*Hedman et al.,* 2013; *Ingersoll and Ewald,* 2017).

5. COMPARISON WITH GEYSERS AND VOLCANIC ERUPTIONS ON EARTH

Several other bodies in the solar system have active plumes. Earth's largest plumes arise from volcanos and are similar to Enceladus only in that they are gas + particulate flows. But Earth's water geysers are perhaps the closest analog to those on Enceladus. However, there are significant differences: Terrestrial geysers are hot (the vapor + droplet emanating flow was not recently in contact with ice), they exhaust into a dense background atmosphere, and gravity dominates the large-scale motions. Entrainment of ambient air and heat exchange with this air dominate the ascent of volcanic plumes (e.g., *Woods,* 1995) and modifies the height and shape of geyser jets (*Karlstrom et al.,* 2013). Enceladus' jets expand into a vacuum and particles should follow ballistic trajectories once they separate from the vapor. A volcanic plume on Io, in contrast, gains a certain relation to the Enceladus plume in that there is no background atmosphere. But ionian plumes also arise from hot rock or lava, sometimes impinging on ice, and are ultimately gravity-dominated. Triton's plumes, though only slightly explored, also rise into a background atmosphere. The suggested Europa south polar plume (*Roth et al.,* 2014; *Sparks et al.,* 2016) may be similar to Enceladus in all but the gravity field and net mass flow. At another end of the spectrum, cometary plumes are similar to the Enceladus plume in terms of their

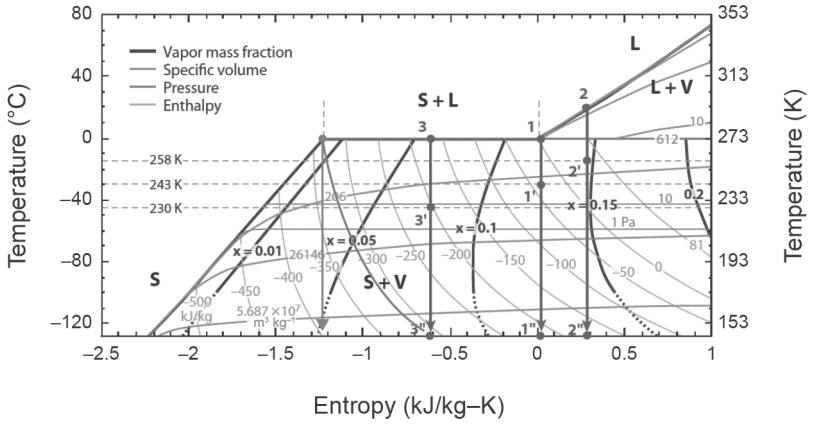

Fig. 11. See Plate 25 for color version. Phase diagram for water at low temperatures and entropies (from *Lu and Kieffer,* 2009). From the red circle to point 1 is liquid water in contact with ice. Isenthalpic (green curve) or isentropic (red line and other vertical lines) decompression increases the mass fraction of vapor (burgundy curves), but only leads to a mass fraction of several percent vapor. In contrast, the plume has an observed vapor mass fraction of 90–95% (e.g., *Gao et al.,* 2016).

gas/particulate dynamics, constituents (*Waite et al.,* 2009), mass flow, velocities, and exhaust into vacuum, but differ in their driving source mechanisms as comets do not have a reservoir of liquid water. The high Mach number narrow jets present on Enceladus and comets indicate that both have vapor expanding through a throat or nozzle. This might be due to the competing effects of condensation and freezing that tend to close a vent opening and the vapor pressure that keeps the vent open or clear.

In terrestrial instances of geologic plumes, eruption speed is usually assumed to be limited to the speed of sound of the gas + particle mixture at the vent (e.g., *Mastin,* 1995) — flow is choked. Observational evidence for choked flow is lacking for magmatic volcanos because the masses of gas and particles are difficult to constrain. Choking has been inferred from measured velocities and vapor-liquid ratios at geysers (*Karlstrom et al.,* 2013; *Munoz-Saez et al.,* 2015), but the uncertainties are large. Establishing that flow is choked is "a notoriously difficult problem" (*Kieffer,* 1989). The observations of high-Mach number vapor (sections 6 and 7) and the collimated particle flow (Fig. 3) on Enceladus, a case in which there is no atmospheric backpressure, are perhaps the strongest observations for choking in natural multiphase eruptions. Important questions are *where* they choke, and whether the flow above that point is reasonably modeled as adiabatic and without much mass exchanged with the conduit walls. If the Enceladus plume nozzles were simply converging nozzles, flow would be sonic at the surface and there would be much expansion of the gas above the surface. The fact that we see particulate beams suggests that that size range of particles we see were beam-formed below the surface. This might have been in a diverging section of the conduit near the surface and the particles became collimated like the gas (see discussion in *Yeoh et al.,* 2015). Or it could have occurred by some process that selectively skimmed laterally moving particles that touched the side walls, irrespective of the gas motion.

The eruptions of magmatic volcanos and geysers on Earth are driven by the volume expansion of gas produced during decompression. Enceladus' eruptions are more similar to geysers, which are one-component systems with mass exchange between liquid, solid, and vapor (Fig. 11), whereas magmatic volcanos only exsolve dissolved gases. Non-condensable gases, such as N_2 and CO_2, have been proposed to play a role in initiating the eruptions of terrestrial geysers (*Lu and Kieffer,* 2009; *Ladd and Ryan,* 2016; *Hurwitz et al.,* 2016), and there are episodically erupting cold geysers driven by CO_2 exsolution (e.g, *Watson et al.,* 2014). The importance of the other gases for boiling geysers, other than slightly changing the liquid stability field, remains unclear (*Hurwitz and Manga,* 2017). The role of observed non-condensable gases [such as CO_2, CH_4, NH_3 and H_2 (*Waite et al.,* 2014)] in eruption processes on Enceladus is also unclear, including their role in driving ascent and sustaining flow within conduits (*Matson et al.,* 2012). But compared to hot geysers on Earth, components dissolved in the cold Enceladus geysers other than H_2O appear to be a larger fraction of the erupted materials.

6. EXPANSION AND ACCELERATION AT THE VENT: GRAIN VELOCITIES, TEMPERATURES, NUCLEATION, AND GROWTH

The observed erupted grains can be separated into three regimes based on their ejected velocity. The slowest group rises out of vents and falls out of the plume in close proximity to the tiger stripes. These particles tend to be large (*Degruyter and Manga,* 2011). Another, faster-moving group, distributes itself broadly over the surface (*Kempf et al.,* 2010). A third group has velocities greater than the escape speed of Enceladus and leaves the satellite altogether. The size and speed relationships of the different populations serve as a diagnostic of the physics of their origins. In this section we discuss the first and second groups of particles

that return to the Enceladus surface; in section 7 we concentrate on the escaping group.

The vapor in a high-Mach-number geyser leaving the surface (region E and beyond, Fig. 9) will be highly supersaturated and will condense on existing ice grains and water droplets (heterogeneous nucleation) to increase their size. There exists a competition, however, between the rapid decrease of gas density that results in a decrease of the rate of molecules colliding with particles (a kinetic limitation), and the growth of the particulate size. *Yeoh et al.* (2015) show that given an assumption of meter-scale vent openings and sonic exit conditions (the throat being at the surface in their discussion), particulates can only grow by at most ~1 μm before the collision rate drops enough to stifle grain growth within several vent diameters of the exit. Condensation of the supersaturated gas may also produce new grains, which range from clusters of a few molecules to several hundred nanometers in size. These nanograins, some of which acquired a charge and were measured by CAPS, are discussed in section 7.

Analyses of CDA *in situ* measurements of grains near Enceladus and in the E ring provide crucial constraints on the size distribution, the velocity distribution, and the sources of the particles. In the E ring, 0.5–2% of the ice grains are rich in sodium salts (*Postberg et al.,* 2009) and have compositions (see the chapter in this volume by Postberg et al.) that confirm Enceladus harbors a subsurface ocean in contact with a rocky core. Near Enceladus, the sodium-rich grains are larger and slower (*Postberg et al.,* 2011), and comprise 99% of the particulate mass ejected from the surface vents (Fig. 12). This is incompatible with non-liquid models for the plume source, and is expected for ice grains that are frozen aerosols or sprays working their way from a liquid ocean to the surface (Schmidt *et al.,* 2008; Spencer et al., this volume). Combining the near-Enceladus and E-ring CDA measurements, *Kempf et al.* (2010) find that the same particle size-and-velocity distributions can explain the particle-size distribution measured over the surface by VIMS (*Jaumann et al.,* 2008), the plume measurements by VIMS and CDA, and the scale height and distribution of particles in the E ring.

Near-infrared spectra of the plume obtained by VIMS provide relatively direct measurements of the size distribution for particles between 1 and 4 μm in radius. The VIMS plume observations are obtained at high phase angles where the signal is primarily due to light diffracting around individual particles. In this limit, a particle of a given radius s observed at a phase angle α scatters light most efficiently at wavelengths $\lambda \sim s/(\pi-\alpha)$. Hence there is a fairly direct mapping between the plume's brightness variations with wavelength and the shape of the particle size distribution. Indeed, *Hedman et al.* (2009) were able to use the VIMS spectra to determine the relative numbers of particles with radii of 1, 2, and 3 μm over a range of altitudes within the plume. This work demonstrated that the number density of 3-μm particles falls much more rapidly with altitude than the number density of 1-μm particles. This implies that the typical launch velocity of 3-μm particles is lower than that of 1-μm particles.

VIMS data can also indicate grain sizes of the large particles on the surface next to the tiger stripes (*Jaumann et al.,* 2008), providing additional constraints on the size of particles that erupt. Deposited ice particles can grow from sputtering (e.g., *Clark et al.,* 1983) or sintering (e.g., *Kaempfer and Schneebeli,* 2007), but at cold surface temperatures these processes may be slow (*Spencer et al.,* 2006) compared to particle deposition times (*Kempf et al.,* 2010). Using the gas flow model of *Ingersoll and Pankine* (2010) and the assumption that the acceleration of particles is limited by the distance they travel between collisions with conduit walls (*Schmidt et al.,* 2008), *Degruyter and Manga* (2011) modeled the acceleration of particles within the conduit and their ballistic transport once they exited the vent — large particles achieve lower exit speeds and hence are transported to lower altitudes and are deposited closer to the vents. *Degruyter and Manga* (2011) fit the predicted transport to the VIMS surface observations of grain sizes in the range of 20–30 μm at distances of 5–10 km from cracks (*Jaumann et al.,* 2008), to determine the relationship between the distance over which particles are accelerated in the conduits and the gas temperature (although grain growth

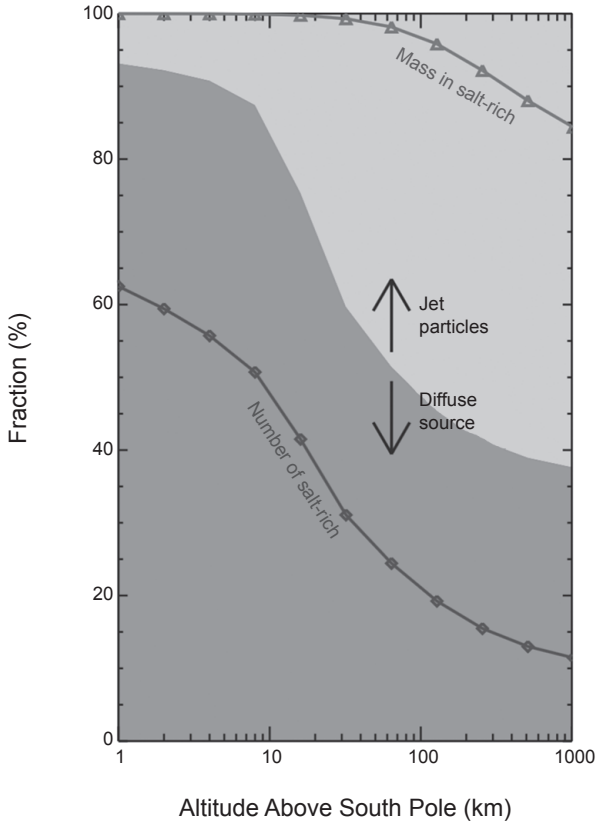

Fig. 12. The fraction of salt-rich grains in the plume decreases with increasing altitude as the larger, slower, salt-rich grains fall back to the surface. Most of the mass of the grains that emerge from the vents is in the larger, salt-rich grains, but most of the grains that escape from Enceladus are salt-poor. From *Postberg et al.* (2011).

through sintering could contribute as well). Figure 13 shows the predicted relationship between particle size and altitude. While the model is constrained only by the surface observations, it is consistent with the high-altitude CDA, VIMS, and E-ring measurements, suggesting that the surface and high-altitude particle sizes originate from the same eruptions but that larger particles move slower than small ones.

Particle-size distributions derived from ISS (visible) images depend on the topology of the particles as smooth spheres interact with light differently than rough-surfaced aggregates of the same size and mass. The *Gao et al.* (2016) analyses of high-phase-angle ISS data show that aggregate models produce grain/vapor ratios of 0.07 ± 0.01, explaining some of the discrepancy between the larger ratios derived from smooth-sphere models (*Ingersoll et al.,* 2010) and the ratios derived from CDA data.

There are two implications of the model and observations of surface grain size. First, particles greater than tens of micrometers erupt, and this is a size greater than what would simply condense from vapor (*Schmidt et al.,* 2008; *Yeoh et al.,* 2015). These large particles may be frozen droplets from the ocean, or mechanically produced particles from the conduit walls. Second, still larger particles may be erupting, but these will remain close to the surface and be deposited close to the surface vents.

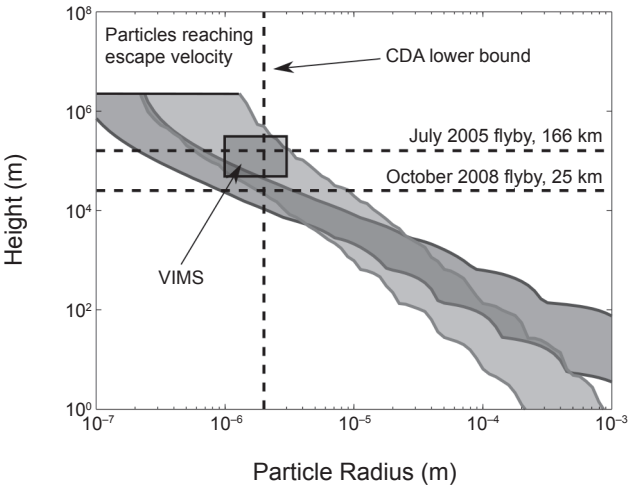

Fig. 13. Maximum particle height as a function of particle size for two models, both constrained by VIMS inferences of particles sizes adjacent to the tiger stripes (*Degruyter and Manga,* 2011). The gray band, which at 1 m height spans particle sizes of 2 × 10^{-4} to 10^{-3} m, indicates acceleration is limited by particle collisions with walls, while in the other band acceleration is limited by gas drag. The region upper and lower bounds for each color are for gas temperatures between 190 K and 273 K. The CDA lower bound is from *Spahn et al.* (2006); the VIMS box is from *Hedman et al.* (2009). The wiggles in the curves arise from the form of the drag model for particles as it transitions from free molecular to transitional to slip flow to continuum flow (*Crowe et al.,* 1997).

7. THE COLLISIONLESS REGIME: SEPARATION OF MOLECULE AND GRAIN MOTION AND MODEL FITS TO IDENTIFY VENT EXHAUST PROPERTIES

CAPS observations of charged nanometer grains in the plume (*Jones et al.,* 2009; *Dong et al.,* 2015) compliment the observations of larger grains discussed in the previous section. CAPS data show a size distribution consistent with condensation during rapid expansion at the surface vent (*Yeoh et al.,* 2015). The observed grains range in size from clusters of a few water molecules to radii of 3 nm, with a peak number density at approximately 2 nm. Particles with sizes between the upper limit (4 nm) of CAPS and the lower limit (0.1 μm) of CDA during Enceladus encounters are likely, but those are unmeasured by Cassini instruments [see *Dong et al.* (2015) for a discussion of the possible distributions between the two size regimes]. The nanometer-sized grains are entrained in the vapor, and accelerate to near-gas velocities as they leave the vent. Most escape Enceladus, but comprise only a small mass fraction of the particulate supply to the E ring. They acquire a charge quickly, and are influenced by Saturn's magnetic field more than the larger particles (see the chapter by Kempf et al. in this volume). Estimates of the total mass of the nanograins range from 1% to 20% of the vapor (*Hill et al.,* 2012; *Dong et al.,* 2015); the large range is due to uncertainties in grain charging and in the CAPS response to nanograins.

The expansion process just above the vents involves a transition from the collisional gas flow regime to a collisionless one. *Yeoh et al.* (2017) showed that if the gas is sufficiently collisional at the vent, the subsequent gas dynamics adiabatic expansion will allow the nearly complete conversion of thermal motion to directed motion and the gas will reach nearly the ultimate speed of $\sqrt{2\gamma RT_0/(\gamma-1)}$. Here, T_0 represents the stagnation temperature of the gas when it was last in thermal equilibrium with liquid or walls of the conduit. If the vent Knudsen number — the ratio of gas mean free path to vent diameter — is too high (greater than ~0.1), residual thermal (random) motion will remain. Hence molecules should reach an ultimate speed limited to about 1005 m s^{-1} by the water triple point temperature of 273 K. Whether the particles follow the gas flow will depend on the local Stokes number, which represents a ratio of grain response time to flow field changes compared to the rate of change of the flow field density along mean streamlines. As described by *Yeoh et al.* (2015), the particle and gas flows decouple at a height of up to 1000 vent diameters for nanometer-sized particles but only perhaps 100 diameters for micrometer-sized particles. Hence, the decoupling happens well below the height at which Cassini actually observed the gas or particulates.

Cassini observed the plume vapor and particulates when both were in the "free molecular" regime — when intermolecular collisions and molecule-particle collisions had ceased to affect molecule and particle trajectories. Hence, the observed characteristics of the plume were imprinted by lower-altitude physics. Those observations may thus be used

to infer the unseen physics and conditions at the vent. In this section, we discuss INMS measurements of the plume vapor distribution, including observations of the broad vapor cloud and discrete gas jets, obtained during these flybys. These *in situ* data, in concert with UVIS stellar and solar occultations of the gas jets, and imaging of the grain jets, provide constraints on the properties (locations, magnitudes, and gas velocity) and time variability of the plume surface sources. Early observations of the gas jets by UVIS, during a plume occultation of the star zeta Orionis on October 24, 2007 (*Hansen et al.,* 2006), showed fine structure in the water vapor density on the scale of a few kilometers in the plume, suggesting the presence of supersonic gas jets having a ratio of bulk velocity to thermal velocity of 1.5 ± 0.2. In the subsequent years, UVIS would acquire several more stellar occultations, and one solar occultation during the May 18, 2010, E10 flyby with exceptionally good signal-to-noise (*Hansen et al.,* 2011), enabling multiple narrow, supersonic jets to be discerned. Additionally, during this time, INMS detection of the individual gas jets required several attempts, over multiple flybys, during which a number of measurement and instrumental challenges were overcome.

The E3 and E5 flybys on March 12, 2008, and October 9, 2008, were the earliest flybys through the plume for which INMS was aimed toward the spacecraft direction of motion to sample and measure the gas density (Fig. 14) and composition (see the chapter in this volume by Postberg et al., as well as Appendix Table A1). These two flybys both took place along similar north-to-south trajectories, and thereby encountered the plume after closest approach, sampling the plume density and composition as the spacecraft moved away from the south polar region. In their analysis of these two flybys, *Teolis et al.* (2010) modeled the adsorption of water vapor on the walls of the INMS gas inlet

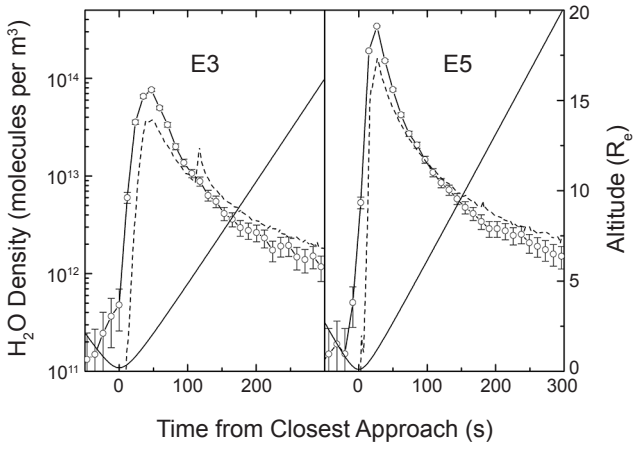

Fig. 14. Plume density (black line, left-axis scale) from models of the INMS measurements of H_2O at mass 18 u (dashed line) vs. time from closest approach for E3 and E5. The solid line shows the altitude (right scale) in Enceladus radii (252 km). Since water is adsorbed to the walls of the INMS inlet aperture, INMS response is delayed and extended compared to the plume density. From *Teolis et al.* (2010).

thermalization antechamber, and found that such sticking introduced a time delay and distortion in the INMS H_2O data. They determined that other plume volatiles including CO_2 vapor provided a more accurate representation of the plume density vs. position along Cassini's trajectory. The CO_2 E3 and E5 data showed that the plume vapor density decays approximately as the inverse square of the distance from the south polar terrain, consistent with collisionless vapor expansion from Enceladus well above the escape speed. Expanding on early UVIS based modeling, *Tian et al.* (2007), *Smith et al.* (2010), *Tenishev et al.* (2010) (both using E3 and E5 INMS data), *Dong et al.* (2011), *Tenishev et al.* (2014), and *Yeoh et al.* (2017) (using UVIS and E3, E5, and E7 INMS data and distributed tiger-stripe sources) applied analytical and Monte Carlo modeling, exemplified in Fig. 15, to estimate plume source properties, i.e., source rate, temperature, and gas velocity, by fitting the eight major grain jets identified from Cassini imagining by *Spitale and Porco* (2007) to these data.

Beginning with the 91-km E7 flyby on November 2, 2009, the Cassini spacecraft carried out a series of low-altitude (<100 km) traversals over the south polar terrain, directly through the plume and sufficiently close to the tiger stripes to observe the detailed spatial distribution or structure of vapor in the gas jets. During these flybys, only the most abundant plume non-sticky species, CO_2 [with a 5% mixing ratio (*Waite et al.,* 2009)], had sufficient signal-to-noise in INMS data to enable accurate measurements of local density variations due to jets along Cassini's trajectory. For the 7.7-km s^{-1} flyby speed and sample cadence of 1.5 s for E7, the spatial resolution of CO_2 measurements was 12 km, which provided only poor resolution of the jets in the E7 data (*Perry et al.,* 2015). To improve resolution in later encounters, the INMS team adjusted the measurement strategy, concentrating the INMS mass scans on the 44-μm CO_2 channels, which yielded CO_2 density data at a higher, 0.25-s temporal and 1.9-km spatial, resolution. As shown in Fig. 16, CO_2 data from E14, E17, and E18 clearly resolved density variations, indicative of gas jets, along Cassini's trajectories. In Fig. 17, we show a three-dimensional projection of these data over the Enceladus south polar terrain, to illustrate how the jet structure observed by INMS is spatially distributed relative to the tiger stripes. Using the E14, E17, and E18 INMS data, *Hurley et al.* (2015a) suggested on the basis of Monte Carlo models that the plume source may be continuously distributed, albeit variable, along the tiger stripes. The complete plume three-dimensional structure is difficult to uniquely constrain solely on the basis of the few INMS flybys as multiple combinations of jet pointing directions and intensities can fit the data, and the jets may be time variable (section 3).

Several groups have modeled the gas density and velocity distributions as the sums of many non-interacting jets emanating from the *Spitale and Porco* (2007) or *Porco et al.* (2014) jets and tiger-stripe fissures. *Teolis et al.* (2017) (with UVIS and INMS data) and *Portyankina et al.* (2016) (using UVIS data) have modeled the plume with all 98 *Porco et al.* (2014)

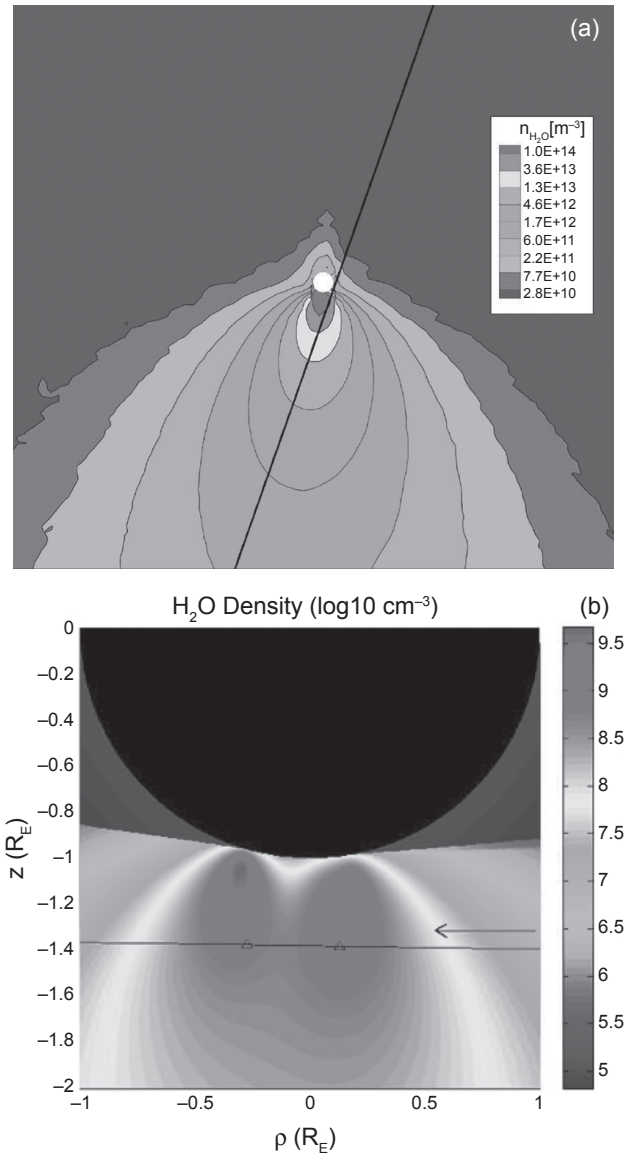

Fig. 15. See Plate 26 for color version. **(a)** Monte Carlo [*Tenishev et al.* (2010) E5 flyby shown] and **(b)** analytical [*Dong et al.* (2011) E7 flyby shown] plume water vapor density models, from fits to INMS E3 and E5 (both models), and E7 [*Dong et al.* (2011) only], with the *Spitale and Porco* (2007) sources as the constraint.

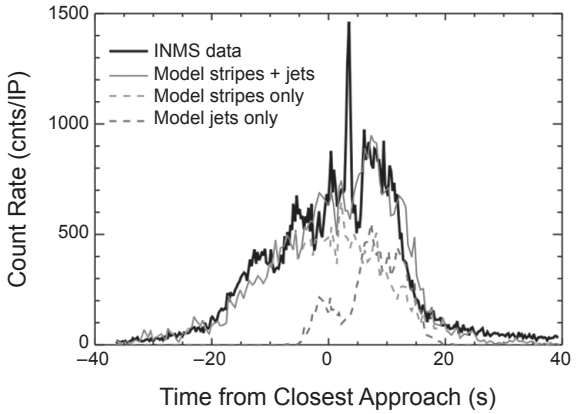

Fig. 16. See Plate 27 for color version. INMS measurements of mass 44 u species during the E17 flyby are shown in black. Model (*Hurley et al.,* 2015) predictions using constant emission along the tiger stripes at 500 m s^{-1} and 270 K (gray dashed line) are selected to match the rise and fall on the outskirts of the plume. The jet model using 1500 m s^{-1} and 270 K are included (blue dashed line) to reproduce the overall enhancement near closest approach. The sum of the two models, shown in red, reproduces the overall structure of the plume but misses some of the fine structure.

jets. *Teolis et al.* (2017) assumed a "drifted Maxwellian" velocity distribution: a random (thermal) spreading superimposed on a bulk velocity. They summed the inputs from separate sources assuming non-interacting (i.e., collisionless) jets, a justified approximation since the jet spacings of a few kilometers are below the ~10-km molecular mean free path at the maximum ~3 × 10^{14} m^{-3} H_2O plume gas densities observed by INMS. *Yeoh et al.* (2017) accounted for intermolecular collisions using well-resolved DSMC simulations for the individual *Spitale and Porco* (2007) jets, including a solution directly coupled to a detailed subsurface simulation.

Modeling results from the INMS team (*Teolis et al.,* 2017) are shown in Fig. 18. Their modeling considers two possible plume contributions: (1) an upward-directed gas source continuously distributed along the tiger stripes, and (2) multiple jets at discrete tiger stripe locations. The jets are given a four-point Mach number distribution ranging from 0 (gas at rest) to 12 (the fast component), as required to best fit the shapes of the features in the six best INMS datasets and two UVIS occultations. Although the fits are not unique, there are only a few families of solutions, and the distribution of Mach numbers is similar among them, with jets with Mach numbers of four or greater required. The fit to the INMS densities and to the UVIS column densities yields broad agreement with the continuous emission model, but the jet model more successfully captures local variations and peaks. The results also suggest stochastic time variability in the plume sources along the tiger stripes. A pattern of systematic variation in specific jets with mean anomaly cannot be presently discerned, probably due to details in the geometry of individual fissures beyond detectability.

Other approaches used a combination of localized jets and continuous emission from the tiger stripes. As an illustration of the quality of the various model fits and to highlight that the models appear to encompass much of the physics to explain the bulk of the observations, we highlight the following: *Hurley et al.* (2015) (Fig. 18) fit the tiger-stripe model to the broad shape of the INMS measurements and used the jets to fit the fine structure. They also investigated the potential for different-mass molecules to have different behavior based on their thermal velocities. *Tenishev et al.* (2014) (Fig. 19) found that simulating the UVIS 2007 occultation data required both jets and continuous tiger stripe emission. *Yeoh et al.* (2017) (Fig. 20) also finds that the best fits require the combination of strong jets and a more-diffuse source from the tiger stripes. Analyses from all these groups used only the *Spitale and Porco* (2008) jets.

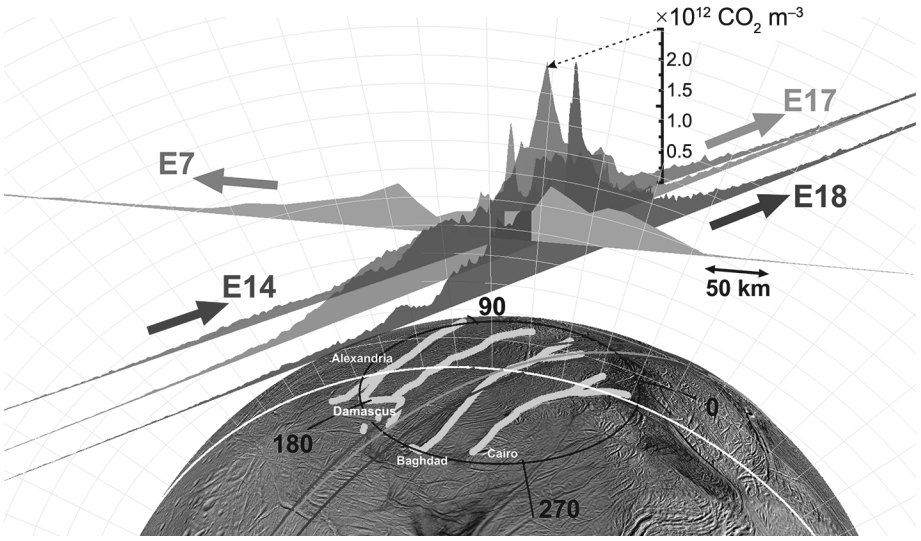

Fig. 17. See Plate 28 for color version. To-scale three-dimensional representation of the E14, E17, E18, and (lower-resolution) E7 INMS data, with vertical areas representing (in linear scale) the density, and the flat base of the areas corresponding to the Cassini trajectories.

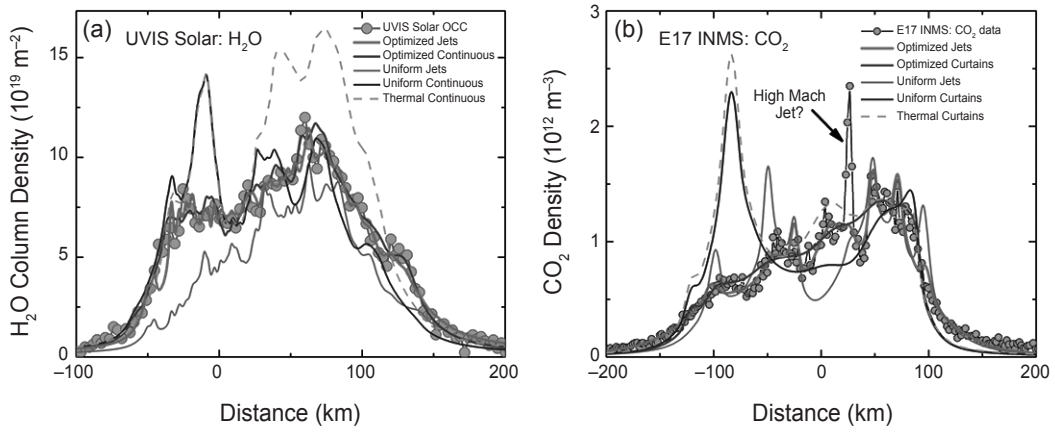

Fig. 18. See Plate 29 for color version. **(a)** Enceladus plume water vapor column density measurement from the UVIS 2010 solar occultation (dotted line), plotted vs. distance across the plume along the occultation line of sight minimum ray height. Thin lines: modeling solutions (*Teolis et al.,* 2017) assuming continuous emission along the tiger stripes. Thick lines: Solutions assuming the *Porco et al.* (2014) jets. **(b)** INMS CO_2 density measurement (dotted line) along the E17 flyby trajectory, showing peaks suggestive of discrete plume sources. Lines: Solutions with *Porco et al.* (2014) jets as the constraint.

During four encounters, INMS used its alternate mode for observing neutrals, the Open Source Neutral Beam (OSNB) mode. During one of encounters, E8, Cassini passes through a jet while rotating so that INMS sampled the water-molecule velocities relative to Enceladus (*Perry et al.,* 2016). The measurements show a bulk velocity of 1.1 ± 0.2 km s^{-1}, which is consistent with the 1.0-km s^{-1} ultimate velocity of adiabatic expansion. During another encounter, E11, similar measurements showed velocities of 600 m s^{-1} outside the strong jets. Combined, these results support the multiple-velocity models of the plume and supply the velocities necessary to interpret the Mach numbers derived from those models. Also, since the different groups did not use a single speed or jet spreading angle for the gas in their models, it is not straightforward to say whether or not simply a difference in assumed/modeled surface exit flow properties is what leads to the different fitted mass fluxes.

8. CONCLUSIONS AND OPEN ISSUES

We list several issues concerning the plume that appear to be resolved by the Cassini observations and modeling but whose resolution itself opens up other questions.

Is Enceladus the dominant source of the E ring? Yes, by ice grains entrained in the plume, not by excavation of grains by micrometeorites, the mechanism proposed before the plumes were discovered (see the chapter in this volume by Dougherty et al.).

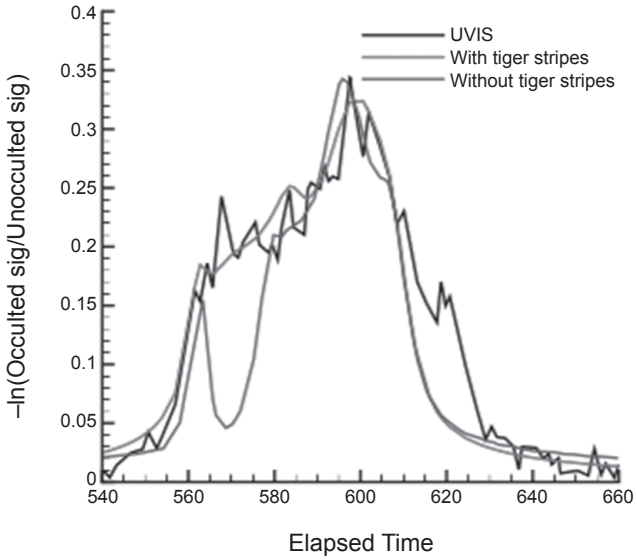

Fig. 19. Comparison of the *Tenishev et al.* (2014) results with the 2010 UVIS solar occultation observation of *Hansen et al.* (2011). Without gas production distributed along the tiger stripes, the model does not reproduce the UVIS scan at the elapsed time of 448.9 s. Gray line with big dip at 570 s: Only the *Spitale and Porco* (2007) sources were used, and the model does not reproduce all the peaks in the UVIS data. Higher-lying gray line: The addition of a tiger stripe gas source to the model is required to fit the data, suggesting additional sources distributed along the tiger stripes as later identified by *Porco et al.* (2014).

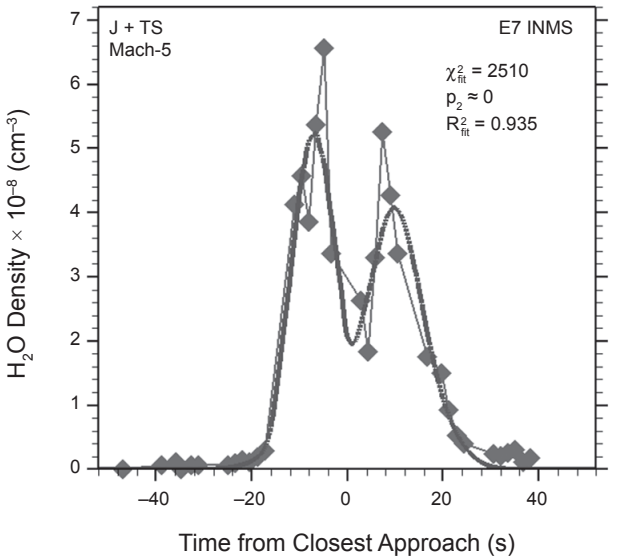

Fig. 20. Best fit of the *Yeoh et al.* (2017) model using Mach 5 exit conditions to the INMS E7 data using both jet and tiger-stripe sources.

Are clathrates the dominant source of the plumes? No. The CDA detection of frozen salty water, combined with gravity data and libration analyses, all point to a subsurface ocean.

Where does the plume originate? From the tiger stripe fractures in the south polar region. Geysers and diffuse sources appear to rise from vents that can be either highly elongated or compact. There remain important questions about the distribution of orifice aspect ratios among the vents.

What is the net mass flow in the plume? Most analyses estimate a few hundred kilograms per second, but there is a factor-of-2 uncertainty in some of the analyses and uncertainty due to the plume variability.

Is the plume just water vapor and ice grains? No, it contains other volatiles and ice particles with several distinct compositional variations. There remain questions about the relative fractions of the constituents and the nature of yet to be identified constituents (see the chapter by Postberg et al. in this volume).

Do the plumes vary, and, if so, over what timescales? Diurnal variations have been observed in the ice-grain flux by VIMS and ISS, and gravitational stress has been identified as the likely cause. ISS imaging and INMS data also give evidence for short-term stochastic variability in discrete sources/jets. But many details remain unknown, for example, the motion of the channel walls and vents that control the flux, the variability of the vapor, and the difference between jet and diffuse variability. The nature of shorter- and longer-term variability also still needs to be fully quantified.

APPENDIX

TABLE A1. Parameters of the Enceladus encounters discussed in this chapter.

Encounter	Date	Minimum Altitude	Features
E0	17 Feb 2005	1259	Magnetometer observations indicated an atmosphere; distant ISS images of plume
E1	9 Mar 2005	497	Imaging, magnetometer, and plasma measurements
E2	14 Jul 2005	168	Relatively far from ejected vapor; minimal data useful for plume structure; first INMS and UVIS identification of H_2O; first CDA measurements of dust; CAPS measurement of plume ions
	24 Oct 2007		UVIS stellar occultation; measurement of high-Mach jets, source rate
E3	12 Mar 2008	51	INMS pass; steeply inclined, fast (14 km s^{-1}) north-south trajectories, following the plume at altitudes more than 250 km
E5	9 Oct 2009	25	INMS pass; steeply inclined, fast (17 km s^{-1}) north-south trajectories, following the plume at altitudes more than 250 km
E7	2 Nov 2009	100	INMS pass; horizontal, slow pass (7 km s^{-1}), low, perpendicular to stripes, outbound from Saturn

TABLE A1 (continued)

Encounter	Date	Minimum Altitude	Features
E8	21 Nov 2009	950	Horizontal, slow pass south of Enceladus 1200 km below the equatorial plane; includes vapor velocity measurements from INMS OSNB data
	18 May 2010		UVIS solar occultation; high-Mach jets; measured source rate
E11	13 Aug 2011		
E14	1 Oct 2011	100	Horizontal, slow pass at low altitude with high-resolution INMS data, parallel to stripes, inbound to Saturn
E16	6 Nov 2011		
E17	27 Mar 2012	75	Horizontal, slow pass at low altitude, high-resolution INMS data, parallel to stripes, inbound to Saturn
E18	14 Apr 2012	75	Horizontal, slow pass at low altitude, high-resolution INMS data, parallel to stripes, inbound to Saturn; last CAPS data
E21	28 Oct 2015	49	Horizontal, slow pass at lowest altitude through plumes, parallel to stripes, INMS OSNB measurements of H_2

REFERENCES

Clark R., Fanale F., and Zent A. (1983) Frost grain size metamorphism: Implications for remote sensing of planetary surfaces. *Icarus, 56,* 233–245.

Crowe C., Sommerfeld M., and Tsuji Y. (1997) *Multiphase Flows with Droplets and Particles.* CRC, Boca Raton, Florida.

Degruyter W. and Manga M. (2011) Cryoclastic origin of particles on the surface of Enceladus. *Geophys. Res. Lett., 38,* L16201, DOI: 10.1029/2011GL048235.

Dong Y., Hill T. W., Teolis B. D., Magee B. A., and Waite J. H. (2011) The water vapor plumes of Enceladus. *J. Geophys. Res., 116,* A10204.

Dong Y., Hill T. W., and Ye S.-Y. (2015) Characteristics of ice grains in the Enceladus plume from Cassini observations. *J. Geophys. Res.–Space Physics, 120,* 915–937, DOI: 10.1002/2014JA020288.

Gao P., Kopparla P., Zhang X., and Ingersoll A. (2016) Aggregate particles in the plumes of Enceladus. *Icarus, 264,* 227–238.

Goguen J. D., Buratti B. J., Brown R. H., Clark R. N., Nicholson P. D., Hedman M. M., Howell R. R., Sotin C., Cruikshank D. P., Baines K. H., Lawrence K. J., Spencer J. R., and Blackburn D. G. (2013) The temperature and width of an active fissure on Enceladus measured with Cassini VIMS during the 14 April 2012 south pole flyover. *Icarus, 226,* 1128–1137.

Hansen C. J., Esposito L., Stewart A. I. F., Colwell J., Hendrix A. P., Shemansky W. D., and West R. (2006) Enceladus' water vapor plume. *Science, 311(5766),* 1422.

Hansen C. J. et al. (2011) The composition and structure of the Enceladus plume. *Geophys. Res. Lett., 38,* L11202.

Hansen C. J., Esposito L. W., Aye K.-M., Colwell J. E., Hendrix A. R., Portyankina G., and Shemansky D. (2017) Investigation of diurnal variability of water vapor in Enceladus' plume by the Cassini ultraviolet imaging spectrograph. *Geophys. Res. Lett., 44,* DOI: 10.1002/2016GL071853.

Hedman M., Nicholson P. D., Showalter M. R., Brown R. H., Buratti B. J., and Clark R. N. (2009) Spectral observations of the Enceladus plume with Cassini-VIMS. *Astrophys. J., 693,* 1749–1762.

Hedman M. M., Gosmeyer C. M., Nicholson P. D., Sotin C., Brown R. H., Clark R. N., Baines K. H., Buratti B. J., and Showalter M. R. (2013) An observed correlation between plume activity and tidal stresses on Enceladus. *Nature, 500,* 182.

Helfenstein P. and Porco C. (2015) Enceladus' geysers: Relation to geological features. *Astron. J., 150,* 96.

Hill T. W., Thomsen M. F., Tokar R. L., Coates A. J., Lewis G. R., Young D. T., Crary F. J., Baragiola R. A., Johnson R. E., Dong Y., Wilson R. J., Jones G. H., Wahlund J.-E., Mitchell D. G., and Horányi M. (2012) Charged nanograins in the Enceladus plume. *J. Geophys. Res., 117,* A05209, DOI: 10.1029/2011JA017218.

Howett C. J. A., Spencer J. R., Pearl J., and Segura M. (2011) High heat flow from Enceladus' south polar region measured using 10–600 cm^{-1} Cassini/CIRS data. *J. Geophys. Res., 116,* E03003.

Hurford T. A., Helfenstein P., Hoppa G. V., Greenberg R., and Bills B. G. (2007) Eruptions arising from tidally controlled periodic openings of rifts on Enceladus. *Nature, 447,* 292–294.

Hurford T. A., Helfenstein P., and Spitale J. N. (2012) Tidal control of jet eruptions on Enceladus as observed by Cassini ISS between 2005 and 2007. *Icarus, 220,* 896–903.

Hurley D. A., Perry M. E., and Waite J. H. (2015) Modeling insights into the locations of density enhancements from the Enceladus water vapor jets. *J. Geophys. Res.–Planets, 120,* 1763.

Hurwitz S. and Manga M. (2017) The fascinating and complex dynamics of geyser eruptions. *Annu. Rev. Earth Planet. Sci., 45,* 31–59.

Hurwitz S., Clor L., McCleskey R. B., Nordstrom D. K., Hune A., and Evans W. (2016) *Dissolved gases in hydrothermal (phreatic) and geyser eruptions at Yellowstone National Park, USA. Geology, 44,* 235. DOI: 10.1130/G37478.1.

Kite E. and Rubin A. (2016) Sustained eruptions on Enceladus explained by turbulent dissipation in tiger stripes. *Proc. Natl. Acad. Sci., 113(15),* 3972–3975.

Ingersoll A. and Pankine A. (2010) Subsurface heat transfer on Enceladus: Conditions under which melting occurs. *Icarus, 206,* 594–607.

Ingersoll A. P. and Nakajima M. (2016) Controlled boiling on Enceladus. 2. Model of the liquid-filled cracks. *Icarus, 272,* 319–326.

Ingersoll A. P. and Ewald S. P. (2011) Total particulate mass in Enceladus plumes and mass of Saturn's E ring inferred from Cassini ISS images. *Icarus, 216(2),* 492–506.

Ingersoll A. P. and Ewald S. P. (2017) Decadal timescale variability of the Enceladus plumes inferred from Cassini images. *Icarus, 282,* 260–275.

Jaumann R. et al. (2008) Distribution of icy particles across Enceladus' surface as derived from Cassini-VIMS measurements. *Icarus, 193,* 407–419.

Jones G. H. et al. (2009) Fine jet structure of electrically charged grains in Enceladus' plume. *Geophys. Res. Lett., 36,* L16204, DOI: 10.1029/2009GL038284.

Kaempfer T. U., and Schneebeli M. (2007) Observations of isothermal metamorphism of new snow and interpretation as a sintering process. *J. Geophys. Res., 112,* D24101, DOI: 10.1029/2007JD009047.

Karlstrom L., Hurwitz S., Sohn R., Vandemeulebrouck J., Murphy F., Rudolph M., Johnston M., Manga M., and McCleskey R. B. (2013) Eruptions at Lone Star Geyser, Yellowstone National Park, USA; 1. Energetics and eruption dynamics. *J. Geophys. Res.–Solid Earth, 118,* 4048-4062.

Kempf S., Beckmann U., and Schmidt J. (2010) How Enceladus dust plume feeds Saturn's E ring. *Icarus, 206,* 446–457.

Kieffer S. W. (1982) Dynamics and thermodynamics of volcanic eruptions — Implications for the plumes on Io. In *Satellites of Jupiter* (D. Morrison, ed.), pp. 647–723. Univ. of Arizona, Tucson.

Kieffer S. W. (1989) Geologic nozzles. *Rev. Geophys., 27(1),* 3–38.

Kliegel J. R. (1963) Gas particle nozzle flow. *Intl. Symposium on Combustion, 9(1),* 811–826.

Ladd B. S. and Ryan M. C. (2016) Can CO_2 trigger a thermal geyser eruption? *Geology, 44(4),* DOI: 10.1130/G37588.1.

Lu X. and Kieffer S. W. (2009) Multicomponent liquid and ice systems on the planets: Thermodynamics and fluid dynamics. *Annu. Rev. Earth Planet. Sci., 37,* 449–477.

Mastin L. G. (1995) *A Numerical Program for Steady-State Flow of Hawaiian Magma-Gas Mixtures Through Vertical Eruptive Conduits*. USGS Open File Report 95-756.

Matson D. L., Castillo-Rogez J. C., Davies A. G., and Johnson T. V. (2012) Enceladus: A hypothesis for bringing both heat and chemicals to the surface. *Icarus, 221,* 53–62.

Mitchell C. J., Porco C. C., and Weiss J. W. (2015) Tracking the geysers of Enceladus into Saturn's E ring. *Astron. J., 149,* 156.

Munoz-Saez C., Manga M., Hurwitz S., Rudolph M., Namiki A., and Wang C-Y. (2015) Dynamics within geyser conduits, and sensitivity to environmental perturbations: Insights from a periodic geyser in the El Tatio geyser field, Atacama Desert, Chile. *J. Volc. Geotherm. Res., 292,* 41–55.

Nakajima N. and Ingersoll A. P. (2016) Controlled boiling on Enceladus. 1. Model of the vapor-driven jets. *Icarus, 272,* 309–318.

Nimmo F., Porco C., and Mitchell C. (2014) Tidally modulated eruptions on Enceladus: Cassini ISS observations and models. *Astron. J., 148,* 46.

Perry M. E., Teolis B. D., Hurley D. M., Magee B. A., Waite J. H., Brockwell T. G., Perryman R. S., and McNutt R. L. (2015) Cassini INMS measurements of Enceladus plume density. *Icarus, 257,* 136.

Perry M. E., Teolis B. D., Grimes J., Miller G. P., Hurley D. M., Waite J. H. Jr., Perryman R. S., and McNutt R. L. Jr. (2016) Direct measurement of the velocity of the Enceladus vapor plumes. *Lunar and Planetary Science XLVII,* Abstract #2846. Lunar and Planetary Institute, Houston, Texas.

Porco C. C., Helfenstein P., Thomas P. C., Ingersoll A. P., Wisdom J., West R., Neukum G., Denk T., Wagner R., Roatsch T., Kieffer S., Turtle E., McEwen A., Johnson T. V., Rathbun J., Veverka J., Wilson D., Perry J., Spitale J., Brahic A., Burns J. A., Del Genio A. D., Dones L., Murray C. D., and Squyres S. (2006) Cassini observes the active south pole of Enceladus. *Science, 311,* 1393–1401.

Porco C., DiNino D., and Nimmo F. (2014) How the geysers, tidal stresses, and thermal emission across the south polar terrain of Enceladus are related. *Astron. J., 148,* 45.

Porco C., DiNino D., and Nimmo F. (2015) Enceladus' 101 geysers: Phantoms? Hardly! Abstract P13A-2118 presented at the 2015 Fall Meeting, AGU, San Francisco, California, December 14–18.

Portyankina G., Esposito L. W., Ali A., and Hansen C. J. (2016) Modeling of the Enceladus water vapor jets for interpreting UVIS star and solar occultation observations. *Lunar and Planetary Science XLVII,* Abstract #2600. Lunar and Planetary Institute, Houston, Texas.

Postberg F., Kempf S., Schmidt J., Brilliantov N., Beinsen A., Abel B., Buck U. and Srama R. (2009) Sodium salts in E-ring ice grains from an ocean below the surface of Enceladus. *Nature, 459,* 1098–1101, DOI: 10.1038/nature08046.

Postberg F., Schmidt J., Hillier S., Kempf S., and Srama R. (2011) A salt-water reservoir as the source of a compositionally stratified plume on Enceladus. *Nature, 474,* 620–622, DOI: 10.1038/nature10175.

Roddier C., Roddier F., Graves J., and Northcott M. (1998) Discovery of an arc of particles near Enceladus' orbit: A possible key to the origin of the E ring. *Icarus, 136(1),* 50–59.

Roth L., Saur J., Retherford K. D., et al. (2014) Transient water vapor at Europa's south pole. *Science, 343(6167),* 171–174.

Saur J., Schilling N., Neubauer F. M., Strobel D. F., Simon S., Dougherty M. K., Russell C. T., and Pappalardo R. T. (2008) Evidence for temporal variability of Enceladus' gas jets: Modeling of Cassini observations. *Geophys. Res. Lett., 35,* L20105, DOI: 10.1029/2008GL035811.

Schmidt J., Brilliantov N., Spahn F., and Kempf S. (2008) Slow dust in Enceladus' plume from condensation and wall collisions in tiger stripe fractures. *Nature, 457,* 685–688.

Smith H. T., Johnson R. E., Perry M. E., Mitchell D. G., McNutt R. L., and Young D. T. (2010) Enceladus plume variability and the neutral gas densities in Saturn's magnetosphere. *J. Geophys. Res., 115,* A10252.

Spahn F. et al. (2006) Cassini dust measurements at Enceladus and implications for the origin of the E ring. *Science, 311,* 1416–1418.

Sparks W. B., Hand K. P., McGrath M. A., Bergeron E., Cracraft M., and Deustua S. (2016) Probing for evidence of plumes on Europa with HST/STIS. *Astrophys. J., 829(2),* 121, DOI: 10.3847/0004-637X/829/2/121.

Spencer J. R. et al. (2006) Cassini encounters Enceladus: Background and the discovery of a south polar hot spot. *Science, 311,* 1401–1405.

Spitale J. N. and Porco C. C. (2007) Association of the jets of Enceladus with the warmest regions on its south-polar fractures. *Nature, 449,* 695.

Spitale J. N., Hurford T. A., Rhoden A. R., Berkson E. E., and Symeon S. P. (2015) Curtain eruptions from Enceladus' south-polar terrain. *Nature, 521,* 57.

Tenishev V., Combi M. R., Teolis B. D., and Waite J. H. (2010) An approach to numerical simulation of the gas distribution in the atmosphere of Enceladus. *J. Geophys. Res., 115,* A09302.

Tenishev V., Ozturk O. C. S., Combi M. R., Rubin M., Hunter J. H., and Perry M. E. (2014) Effect of the tiger stripes on the water vapor distribution in Enceladus' exosphere. *J. Geophys. Res.–Planets, 119,* 2658.

Teolis B. D., Perry M. E., Magee B. A., Westlake J., and Waite J. H. (2010) Detection and measurement of ice grains and gas distribution in the Enceladus plume by Cassini's Ion Neutral Mass Spectrometer. *J. Geophys. Res., 115,* A09222.

Teolis B. D., Perry M. E., Hansen C. J., Waite J. H., Porco C. C., Spencer J. R., and Howett C. J. A. (2017) Enceladus plume structure and time variability: Comparison of Cassini observations. *Astrobiology, 17(9),* DOI: 10.1089/ast.2017.1647.

Tian F., Stewart A. I. F., Toon O. B., Larsen K. W., and Esposito L. W. (2007) Monte Carlo simulations of the water vapor plumes on Enceladus. *Icarus, 188,* 154.

Waite J. H. et al. (2009) Liquid water on Enceladus from observations of ammonia and ^{40}Ar in the plume. *Nature, 460,* 487.

Waite J. H., Glein C. R., Perryman R. S., Teolis B. D., Magee B. A., Miller G., Grimes J., Perry M. E., Miller K. E., Bouquet A., Lunine J. I., Brockwell T., and Bolton S. J. (2017) Cassini finds molecular hydrogen in the Enceladus plume: Evidence for hydrothermal processes. *Science, 356(6334),* 155–159, DOI: 10.1126/science.aai8703.

Watson Z. T., Han W. S., Keating E. H., Jung N. H., and Lu M. (2014) Eruption dynamics of CO_2 driven cold-water geysers: Crystal, Tenmile geysers in Utah and Chimayó geyser in New Mexico. *Earth Planet. Sci. Lett., 408,* 272–284.

Woods A.W. (1995) The dynamics of explosive volcanic eruptions. *Rev. Geophys., 33,* 495–530.

Yeoh S. K., Chapman T., Goldstein D., Varghese P., and Trafton L. (2015) Understanding the physics of Enceladus south polar plume via direct numerical simulation. *Icarus, 253,* 205–222, DOI: *10.1016/j.icarus.2015.02.020.*

Yeoh S. K., Li Z., Goldstein D. B., Varghese P. L., Levin D. A., and Trafton L. M. (2017) Constraining the Enceladus plume using numerical simulation and Cassini data. *Icarus, 281,* 357.

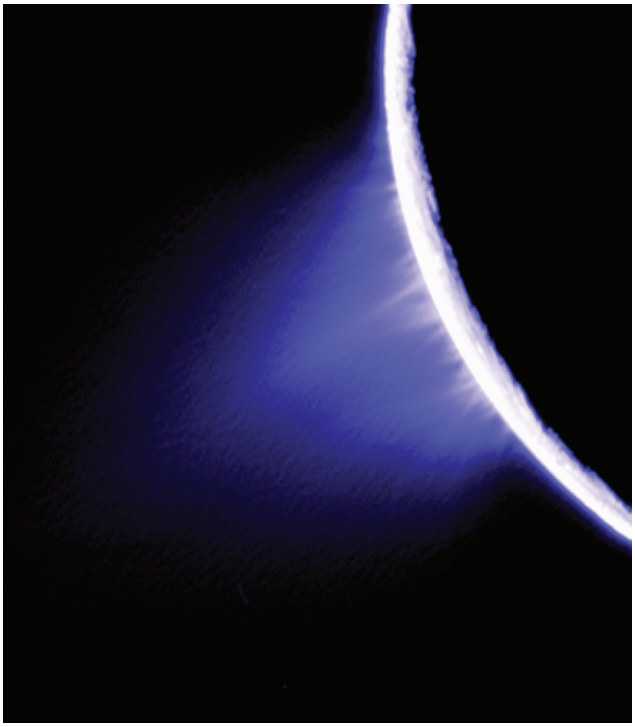

Plate 21. An ISS color-stretched image acquired on November 27, 2005, illustrating overall plume morphology threaded by many finely resolved jets or geysers.

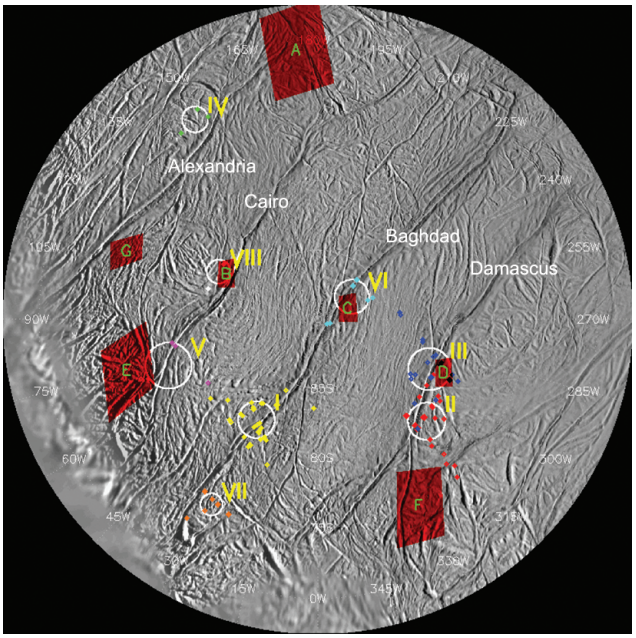

Plate 22. Polar stereographic projection of Enceladus' south polar region showing the eight source locations inferred by *Spitale and Porco* (2007) using triangulation. Locations of CIRS hot spots from *Spencer et al.* (2006) are shown as red quadrilaterals.

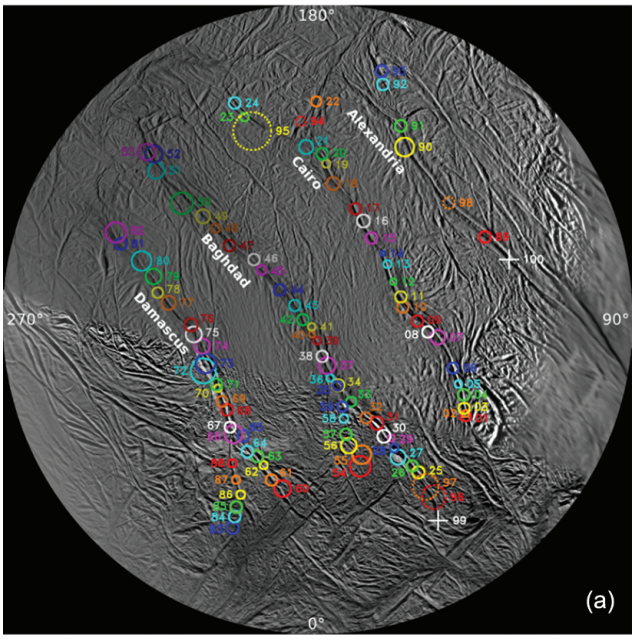

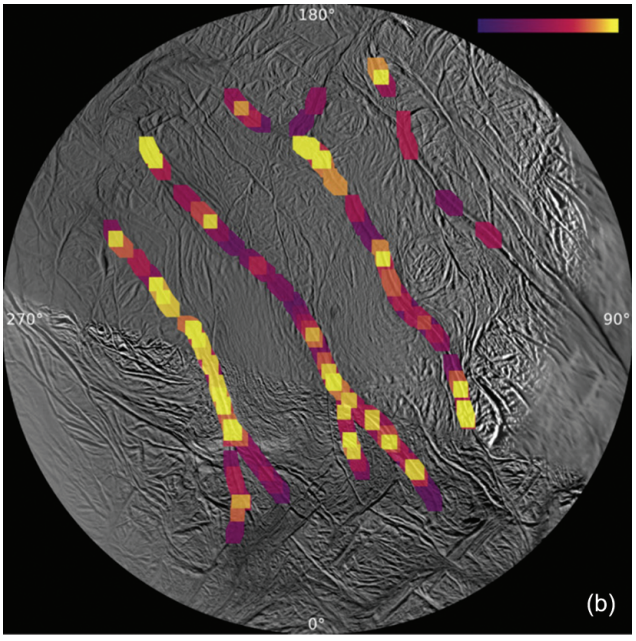

Plate 23. (a) Locations of the jets. **(b)** Jet activity derived from ISS observations. There is strong correlation with the jet activity and the tiger-stripe temperatures measured by CIRS and VIMS. From *Porco et al.* (2014).

Plates accompany chapter by Goldstein et al. (pp. 175–194).

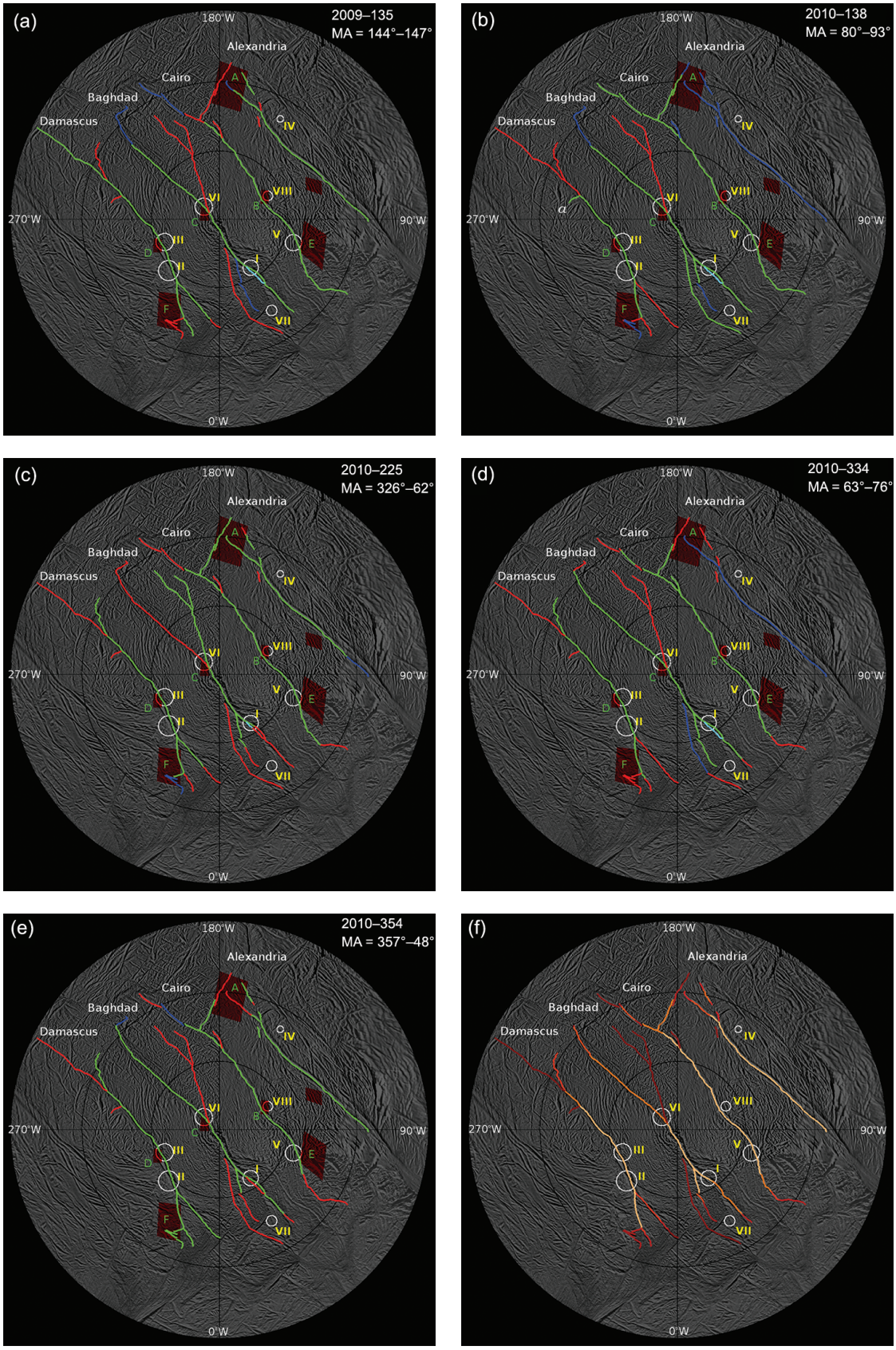

Plate 24. Curtain activity at five different mean anomalies (MA), and the average (f). Green areas are active, red areas are inactive, and blue areas are undetermined.

Plates accompany chapter by Goldstein et al. (pp. 175–194).

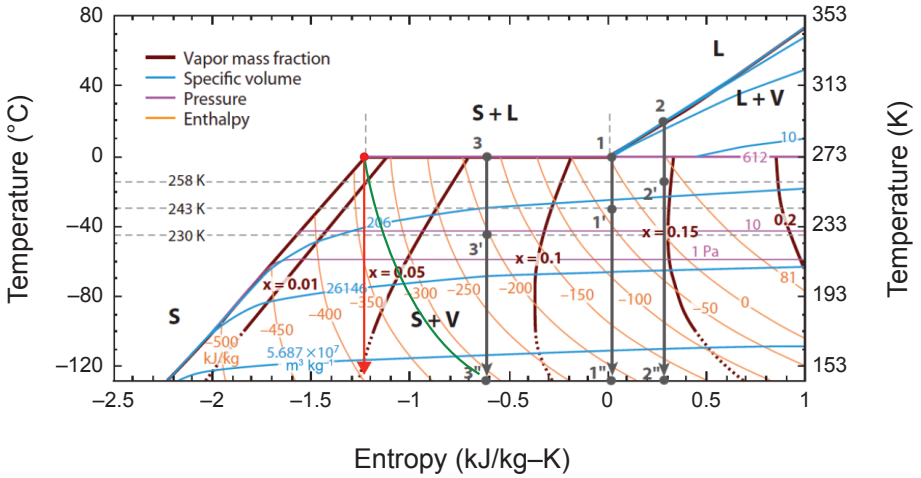

Plate 25. Phase diagram for water at low temperatures and entropies (from *Lu and Kieffer,* 2009). From the red circle to point 1 is liquid water in contact with ice. Isenthalpic (green curve) or isentropic (red line and other vertical lines) decompression increases the mass fraction of vapor (burgundy curves), but only leads to a mass fraction of several percent vapor. In contrast, the plume has an observed vapor mass fraction of 90–95% (e.g., *Gao et al.,* 2016).

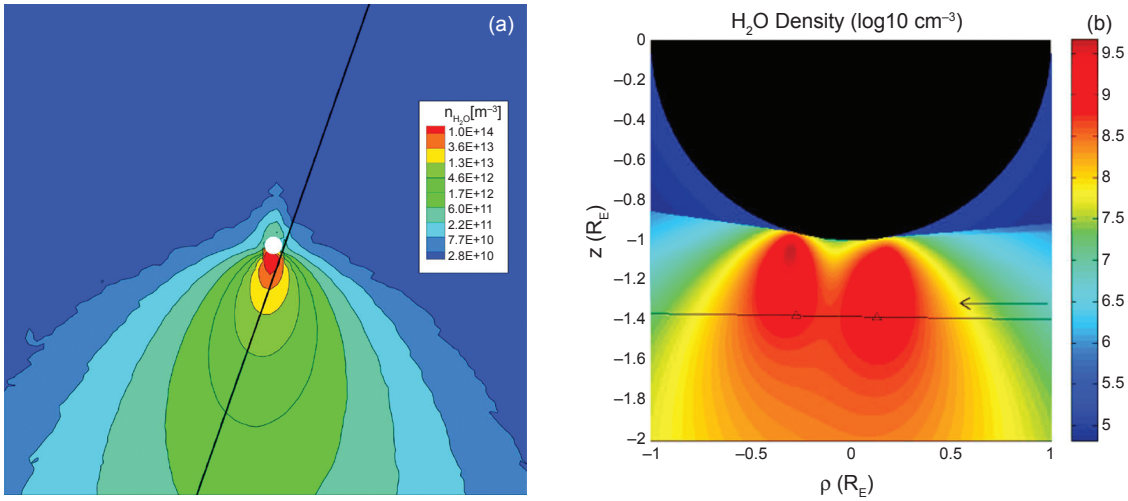

Plate 26. (a) Monte Carlo [*Tenishev et al.* (2010) E5 flyby shown] and **(b)** analytical [*Dong et al.* (2011) E7 flyby shown] plume water vapor density models, from fits to INMS E3 and E5 (both models), and E7 [*Dong et al.* (2011) only], with the *Spitale and Porco* (2007) sources as the constraint.

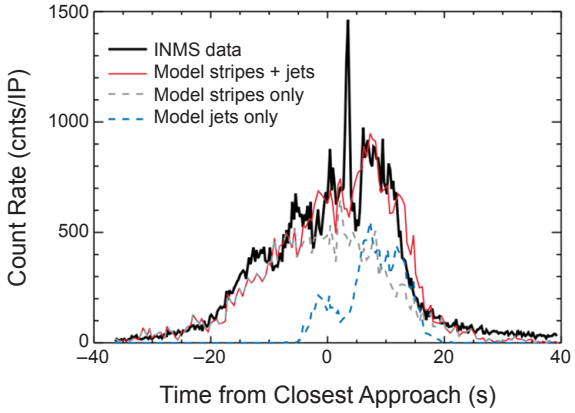

Plate 27. INMS measurements of mass 44 u species during the E17 flyby are shown in black. Model (*Hurley et al.,* 2015) predictions using constant emission along the tiger stripes at 500 m s^{-1} and 270 K (gray dashed line) are selected to match the rise and fall on the outskirts of the plume. The jet model using 1500 m s^{-1} and 270 K are included (blue dashed line) to reproduce the overall enhancement near closest approach. The sum of the two models, shown in red, reproduces the overall structure of the plume but misses some of the fine structure.

Plates accompany chapter by Goldstein et al. (pp. 175–194).

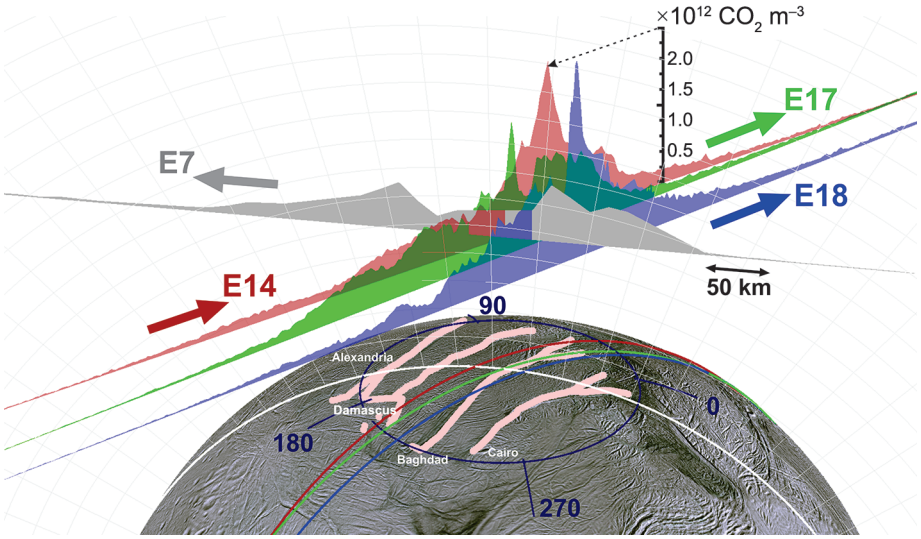

Plate 28. To-scale three-dimensional representation of the E14, E17, E18, and (lower-resolution) E7 INMS data, with vertical areas representing (in linear scale) the density, and the flat base of the areas corresponding to the Cassini trajectories.

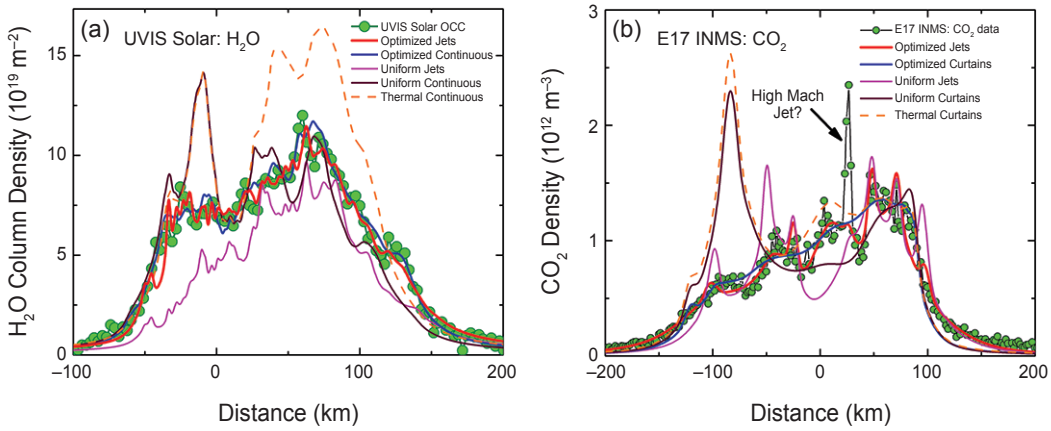

Plate 29. (a) Enceladus plume water vapor column density measurement from the UVIS 2010 solar occultation (dotted line), plotted vs. distance across the plume along the occultation line of sight minimum ray height. Thin lines: modeling solutions (*Teolis et al.,* 2017) assuming continuous emission along the tiger stripes. Thick lines: Solutions assuming the *Porco et al.* (2014) jets. **(b)** INMS CO_2 density measurement (dotted line) along the E17 flyby trajectory, showing peaks suggestive of discrete plume sources. Lines: Solutions with *Porco et al.* (2014) jets as the constraint.

Plates accompany chapter by Goldstein et al. (pp. 175–194).